

Theranostics

2026; 16(4): 1762-1781. doi: 10.7150/thno.113347

Research Paper

A novel TM4SF4-targeting therapeutic antibody candidate with antitumor activity by blocking IGF1R and CD44 signaling and downregulating PD-L1 and B7-H4

Rae-Kwon Kim 1,2* , Chang-Kyu Heo 3* , Mun Ju Choi 4* , Yeon-jee Kahm 1,5 , Min Kyu Kim 4 , Minyong Lee 4 , Ji Yoon Lee 4 , Hwangseo Park 4 , Uhee Jung 1 , Byung-Chul Shin 1 , Bum-Jin Kim 6 , Sung-Chul Kim 6 , Eun-Wie Cho 3 , Chun Jeih Ryu 4 , In-Gyu Kim 1,5

- Department of Radiation Biology, Environmental Radiation Research Group, Korea Atomic Energy Research Institute (KAERI), Daejeon 34057, Republic of Korea.
- 2. Department of Biotechnology, Yong In University, 134, Yongindaehak-ro, Cheoin-gu, Yongin-si, Gyeonggi-do, 17092, Republic of Korea.
- 3. Infectious Disease Research Center, Korea Research Institute of Bioscience and Biotechnology (KRIBB), Daejeon 34141, Republic of Korea.
- 4. Department of Integrative Bioscience and Biotechnology, Institute of Bioscience, Institute of anticancer medicine development, Sejong University, Seoul 05006, Republic of Korea.
- 5. Department of Radiation Life Science, Korea University of Science and Technology (UST), Daejeon 34113, Republic of Korea.
- Algok Bio Inc. 320 120th Ave. NE #208 Bellevue, WA 98005, USA.
- * Rae-Kwon Kim, Chang-Kyu Heo, and Mun Ju Choi contributed equally to this manuscript and have the same first authority.
- ☑ Corresponding authors: Eun-Wie Cho, Infectious Disease Research Center, Korea Research Institute of Bioscience and Biotechnology, 125 Gwahak-ro, Yuseong-gu, Daejeon 34141, Republic of Korea, Phone: +82-42-860-4155, E-mail: ewcho@kribb.re.kr; Chun Jeih Ryu, Department of Integrative Bioscience and Biotechnology, Sejong University, 209 Neungdong-ro, Gwangjin-gu, Seoul 05006, Republic of Korea, Phone: +82-2-3408-3718, E-mail: cjryu@sejong.ac.kr; In-Gyu Kim, Department of Radiation Life Science, Korea University of Science and Technology (UST), Daejeon 34113, Republic of Korea. +82-42-868-8030, E-mail: igkim@ust.ac.kr.
- $\[mathcase]$ The author(s). This is an open access article distributed under the terms of the Creative Commons Attribution License (https://creativecommons.org/licenses/by/4.0/). See https://ivyspring.com/terms for full terms and conditions.

Received: 2025.03.06; Accepted: 2025.10.28; Published: 2026.01.01

Abstract

Rationale: Transmembrane 4 superfamily member 4 (TM4SF4) has been identified as a key regulator of epithelial-mesenchymal transition (EMT)-associated stemness in non-small cell lung cancer (NSCLC) cells through autocrine signaling involving insulin-like growth factor 1 (IGF1) and osteopontin (OPN). Given its pivotal role in tumor progression and therapy resistance, TM4SF4 represents a promising therapeutic target.

Methods: To develop a therapeutic antibody against TM4SF4, we generated anti-TM4SF4 monoclonal antibodies in mice by targeting the large extracellular loop (LEL) of human TM4SF4 using a 15-mer peptide, hTM4SF4 (T126–E140). Among the generated clones, the 2B7 antibody exhibited high specificity and reactivity to TM4SF4. Mechanistic studies were conducted to evaluate the effects of 2B7 on key signaling pathways, EMT-associated stemness, immune checkpoint ligand (ICL) expression, and immune responses. To facilitate clinical translation, 2B7 was humanized, generating the Hz2B7-1.1 antibody, which underwent affinity maturation to select the lead candidate, Hz2B7-1.2. Functional assays, including antibody-dependent cellular cytotoxicity (ADCC) and preclinical evaluations in xenograft models, were performed to assess its therapeutic potential.

Results: The 2B7 antibody demonstrated significant antitumor efficacy in both A549 xenograft and patient-derived xenograft (PDX) models. Mechanistically, 2B7 inhibited key signaling pathways, including PI3K/AKT/GSK3β/β-catenin and JAK2/STAT3, leading to a reduction in EMT-associated stemness and therapy resistance. Additionally, 2B7 downregulated the expression of ICLs, such as PD-L1 and B7-H4, promoting T-cell activation and mitigating immune evasion. Furthermore, 2B7 reduced the secretion of exosomal ICLs by tumor cells and enhanced antitumor immune responses. The humanized antibody Hz2B7-1.2 retained binding properties and antitumor activity comparable to the parental 2B7 antibody and effectively induced ADCC as an IgG1-type antibody.

Conclusions: The humanized anti-TM4SF4 antibody, Hz2B7-1.2, exhibits strong antitumor activity through multiple mechanisms, including inhibition of oncogenic signaling pathways, reduction of EMT-associated stemness, and modulation of immune responses. These findings support Hz2B7-1.2 as a promising therapeutic candidate for TM4SF4-positive cancers, warranting further clinical investigation.

Keywords: TM4SF4, EMT-associated stemness, monoclonal antibody (2B7), humanized antibody (Hz2B7-1.2), signaling blocking

Introduction

Lung cancer is the most common cancer and the leading cause of cancer-related deaths worldwide [1]. Non-small cell lung cancer (NSCLC) accounts for over 75% of all lung cancer cases and remains one of the most difficult to treat because of its high resistance to conventional therapies such as chemotherapy, y-radiation, and targeted therapy [2,3]. Recently, immunotherapy using immune checkpoint inhibitors (ICIs) has significantly improved the outcomes of NSCLC, extending survival in approximately 20% of patients [4]. However, resistance to immunotherapy has become a major challenge, necessitating new strategies to overcome disease progression [4,5]. A comprehensive understanding of the mechanisms underlying therapy resistance-including resistance to immunotherapy – and poor prognosis in NSCLC is essential for the development of effective treatments [6].

PD-L1 (B7-H1) is a transmembrane immune checkpoint ligand that is expressed in cancer and hematopoietic cells. By binding to the PD-1 receptor on immune cells such as T cells, PD-L1 suppresses immune activation and promotes cancer immune evasion [7]. PD-L1 is frequently upregulated in various cancers, including triple-negative breast cancer and NSCLC [8,9]. Similarly, B7-H4, another B7 family ligand, negatively regulates T-cell responses and is overexpressed in cancers, including lung cancer, correlating with poor outcomes [10,11]. Therefore, targeting B7 ligands or their receptors is a promising strategy to overcome T cell anergy and restore antitumor immunity. Antibodies against PD-1, and PD-L1—collectively known CTLA-4, ICIs-have demonstrated substantial efficacy in treating cancers, such as melanoma and lung cancer [12,13], while therapies targeting B7-H4 are entering clinical trials [14]. To further enhance ICI efficacy, it is important to understand the regulatory mechanisms governing PD-L1 and B7-H4 expression in cancer cells.

Cancer stem cells (CSCs) play a critical role in shaping the tumor immune microenvironment and contribute resistance to ICI [15,16]. Epithelial-to-mesenchymal transition (EMT), which is closely linked to increased expression of immune checkpoint molecules, represents another potential mechanism of immune escape [17]. Conversely, mesenchymal-to-epithelial transition (MET) has been proposed as a strategy to sensitize tumors to ICIs [18]. Thus, targeting CSCs and modulating EMT/MET dynamics may improve ICI efficacy by overcoming immune resistance mechanisms [19].

The tetraspanin TM4SF family plays a crucial

role in signaling pathways that regulate cell growth, migration, and development [20]. Among its members, TM4SF1 and TM4SF5 are frequently overexpressed in various tumors, including hepatocellular carcinoma (HCC) and prostate cancer, where they promote EMT-associated signaling and are regarded as important therapeutic targets [21-23]. TM4SF4, another member of the TM4SF family, is overexpressed in HCC and colorectal cancer [24,25]. Suppression of TM4SF4 significantly inhibits HCC cell growth, underscoring its potential as a target for preventing tumor progression [26]. In our previous study using lung adenocarcinoma cells, we found that overexpressed TM4SF4 recruits IGF1R, leading to activation of IGF1Rβ and downstream PI3K/AKT/GSK3 β / β -catenin pathway, which is correlated with poor patient prognosis [27,28]. TM4SF4 overexpression also enhances the autocrine feedback loop of osteopontin (OPN) and insulin-like growth factor 1 (IGF1), ligands that activate the CD44 and IGF1Rβ signaling pathways [28]. Alongside IGF1/IGF1R signaling, OPN/CD44 binding activates JAK2 (or FAK)/STAT3 pathways, promoting EMT-associated CSC properties, tumor metastasis, and v-radiation resistance [28,29]. TM4SF4 is also overexpressed in ALDH1high CSC-like cells [28]. These observations suggest that TM4SF4 is a promising molecular target, particularly in therapy-resistant CSC-like cancers.

Monoclonal antibodies (mAbs) serve as both diagnostic and therapeutic agents owing to their high target specificity and stability in vivo [30]. Since the introduction of the first therapeutic mAb in 1986 [31], mAb development has rapidly progressed, with over 183 approved products and more than 1,200 in clinical development (see: https://www.antibodysociety .org/resources/approved-antibodies) [32]. murine mAbs are easy to produce, their therapeutic use in humans is limited by the human anti-mouse antibody (HAMA) response, which reduces efficacy and increases immunogenicity [33]. To address this, humanized mAbs were developed by grafting murine complementarity-determining regions (CDRs) onto a human antibody framework in a process known as CDR grafting [34]. However, simple CDR grafting can reduce affinity, as some framework region (FR) residues directly interact with the antigen or stabilize the CDR loop conformation [35]. Affinity maturation is commonly implemented to optimize therapeutic mAbs, enhancing their binding kinetics and affinity [36,37], usually by introducing targeted mutations in CDR or FR residues informed by the structure of the antigen-antibody complex [38].

In this study, we developed a murine monoclonal antibody targeting human TM4SF4

(anti-hTM4SF4 mAb), designated 2B7, which exhibited potent anti-cancer effects in NSCLC both *in vitro* and *in vivo*. We demonstrated that the anti-cancer efficacy of 2B7 is mediated by the inhibition of the IGF1/IGF1R β and OPN/CD44 signaling, both central to cancer stem cell regulation, and by suppressing immune evasion via downregulation of PD-L1 and B7-H4. To enable clinical application of the highly active murine 2B7 antibody, we generated a humanized version through CDR grafting and affinity maturation, and evaluated its therapeutic potential as an anti-cancer agent. Finally, we discuss the future development and clinical application of humanized 2B7 antibodies.

Methods

Chemicals and antibodies

All chemicals used were of reagent grade or higher. The antibodies used for western blotting and immunofluorescence assays are listed in Table S1.

Cell culture and transfections

HEK293T (CRL-3216), A549 (CCL-185), and THLE-2 (CRL-2706) cells were obtained from ATCC, while Calu-3, Huh7, and MIA PaCa-2 cells were from KCLB. Human primary hepatocytes were purchased from Thermo Fisher Scientific. Cells were cultured in DMEM or RPMI-1640 medium (Biowest) with 10% FBS (VWR) and antibiotic-antimycotic solution (Welgene) at 37°C, 5% CO₂, unless otherwise specified. THLE-2 cells were cultured in BEBM medium (Lonza) with SingleQuots Supplement Pack (excluding gentamycin/ amphotericin and epinephrine) supplemented with 5 ng/mL EGF, 70 ng/mL phosphoethanolamine. Murine hybridomas were cultured in DMEM supplemented with HT (Sigma-Aldrich). **DHFR-deficient** medium CHO-DG44 cells [39] were maintained in DMEM/F12 (Welgene) with HT medium. For DHFR⁺ selection, CHO-DG44 cells were cultured in IMDM (Welgene) with 100 µg/mL G418 (Duchefa). The hTM4SF4 (NM_004617.4) gene was cloned into pEGFP-C2 or p3xFLAG-CMV 7.1 vectors and transfected into HEK293T cells using Lipofectamine 2000 (Invitrogen). TM4SF4-targeting (5'-CACCUUUCCCAAGAGAUCU-3') and negative control siRNA (Invitrogen) were transfected using Lipofectamine RNAiMAX (Invitrogen). Cells were analyzed 48 h post-transfection.

Production of murine anti-hTM4SF4 monoclonal antibodies

Monoclonal antibodies (mAbs) targeting LEL of hTM4SF4 (UniProt: P48230) were generated using a

synthetic peptide hTM4SF4 (T126-E140: TWGYPFHDGDYLNDE) modified with N-terminal cysteine and conjugated to BSA via sulfo-SMCC (Thermo Fisher Scientific). BALB/c mice were immunized, and hybridomas were produced following AbClon (Korea) protocols. Anti-hTM4SF4 hybridomas were screened by ELISA, and the were purified using protein antibodies chromatography (Cytiva). Purity was confirmed by SDS-PAGE, followed by Coomassie Blue staining.

cDNA synthesis and CDR sequencing of the 2B7 antibody

Total RNA was extracted from 2B7 hybridoma cells using RNAiso Plus (TaKaRa) and cDNA was synthesized using PrimeScriptTM RT Master Mix (TaKaRa). Antibody variable region cDNAs were amplified using modified primers based on a previously reported method [40]. For amplification, 5' MH1/MH2 and 3' IgG1 primers were used for the heavy chain, while 5' MK and 3' Ck primers were used for the light chain. The amplified cDNAs were digested, subcloned into pBluescript KS(+) and sequenced (Bionics).

Chimeric and humanized 2B7 antibody generation and characterization

The chimeric 2B7 antibody was generated by fusing variable heavy (VH) and variable kappa (VK) region DNA sequences with murine signal peptides via recombinant PCR (primers: Table S2) and subcloning into the pdCMV-dhfr vector [41], yielding pdCMV-dhfr-Chi2B7. For antibody humanization, BLAST analysis identified 3QRG_H and 3QRG_L as the most homologous human frameworks to the 2B7 VH and Vk regions [42]. 2B7 CDRs were grafted onto these frameworks via DNA synthesis. The humanized VH gene (Hz2B7-1.0) was generated by recombinant PCR (primers: Table S3), while the humanized Vk was synthesized gene (Hz2B7-0.1)chemically (Bionics). Both genes were subcloned pdCMV-dhfr, yielding the Hz2B7-1.1 expression vector. To enhance the antigen-binding activity of the affinity maturation Hz2B7-1.1 antibody, performed using a docking simulation model of the antigen-antibody complex. Specific residues in the Hz2B7-1.1 heavy and light chains were mutated via recombinant PCR with synthetic oligonucleotides (Table S4). The resulting expression vectors were transiently transfected into HEK293T cells using polyethyleneimine (Polyscience) and TOM medium (Welgene). Antibodies were purified from culture supernatants via protein G chromatography and analyzed by SDS-PAGE and western blotting with anti-human IgG-HRP antibodies (Thermo Fisher

Scientific).

Homology modeling and docking simulation of the 2B7 antibody

Because the 3D structure of the 2B7 antibody was unavailable, homology modeling was performed using the X836 antibody (PDB: 3MBX) as a template [43]. Sequence alignment was conducted using ClustalW [44] and the structural model was built using MODELLER [45]. Molecular dynamics (MD) simulations were employed to refine the model, with regions reconstructed via enumeration algorithms to account for structural flexibility [46]. The hTM4SF4 (T126-E140) peptide structure was optimized through energy minimization. homology-modeled 2B7 antibody structure served as the receptor model for epitope interaction simulations. Docking simulations within the 2B7 CDR were conducted using AutoDock [47] to evaluate the binding affinity and interaction modes. A modified binding energy function incorporating a ligand dehydration term was applied to improve interaction estimation [48]. Among the 20 epitope conformations generated, the lowest binding free conformation was selected as the final binding mode.

Generation of high-producing antibody clones

CHO-DG44 cells were transfected Pvul-digested antibody expression vectors using Lipofectamine 2000 and TOMTM medium. After 48 h, cells were seeded into 96-well plates (7×10³ cells/well) with selection medium (IMDM, 10% FBS, 100 µg/mL G418). Neomycin-resistant clones were screened by sandwich ELISA after three weeks, high-producing clones were expanded in 24-well under 0.02 µM methotrexate Sigma-Aldrich) selection. The selection was repeated with 0.08 µM MTX. Finally, high-producing cells were expanded, and antibodies were purified via protein G chromatography.

Indirect ELISA

hTM4SF4 (T126–E140)-conjugated BSA (50 ng/well or 100 ng/well) was coated onto Maxisorp 96-well plates (Thermo Fisher Scientific). After blocking with 1% BSA in TBST (TBS containing 0.05% Tween-20), the plates were incubated with primary antibodies for 2 h at 37°C. HRP-conjugated anti-mouse IgG antibody (CST) or HRP-conjugated goat α-human IgG-kappa chain antibody (Bethyl) were used as the secondary reagents. The reaction was developed using Ultra-TMB solution (Thermo Fisher Scientific) or OPD substrate (Sigma-Aldrich), and absorbance was measured at 450 nm or 490 nm using a microplate reader.

Western blot analysis and immunoprecipitation

Cell extracts were prepared using RIPA buffer (PBS, pH 7.4, with 1.0% NP-40, 0.1% SDS, and 0.5% deoxycholate) supplemented phosphatase and protease inhibitors (Roche). For immunoprecipitation (IP), 500 µg of RIPA lysates p3xFLAG-TM4SF4-transfected cells incubated with specific antibodies at 4°C for 16 h, followed by Protein G bead capture. For western blot (WB), cell lysates or immunoprecipitates were separated by SDS-PAGE, transferred to PVDF membranes, blocked with 10% non-fat milk in TBST, and incubated with primary antibodies overnight at 4°C. HRP-linked secondary antibodies were applied, and signals were detected using an ECL HRP substrate.

Fluorescence microscopy

Transfected HEK293T or A549 cells were cultured on glass coverslips placed in 35 mm culture plates, fixed with 4% paraformaldehyde (PFA) (Sigma-Aldrich), and incubated overnight at 4°C with specific antibodies in TBS (pH 7.4). Fluorescent staining was performed using either rhodamine-conjugated anti-mouse IgG+IgM+IgA antibody (Abcam) or Alexa Fluor 488-conjugated anti-rabbit IgG antibody (Invitrogen). Nuclei were counterstained with DAPI, and fluorescence images were acquired using a Zeiss LSM510 Meta confocal microscope (Carl Zeiss MicroImaging GmbH).

Surface Plasmon resonance (SPR) analysis

Binding affinity of anti-TM4SF4 antibodies to the hTM4SF4 (T126–E140) peptide was evaluated using a Biacore T200 system (Cytiva). A biotinylated hTM4SF4 peptide containing a GSAGGS spacer was immobilized on a streptavidin-coated sensor chip (Cytiva). Antibodies were prepared in a two-fold serial dilution series (128–1 nM or 512–16 nM) using HBS-EP+ buffer (Cytiva). SPR measurements were performed at 25°C with a flow rate of 30 μ L/min, and affinity constants were determined using Biacore T200 Evaluation Software 3.1 with a 1:1 binding model.

Tumor cell-based assays

For colony formation assays, 1×10^3 cells were seeded in 35-mm dishes and treated with 2B7 antibody (5 µg/mL) or control IgG with or without γ -radiation (6 Gy). After 10–14 days, colonies were stained with crystal violet and counted. For sphere formation assays, 1–2 cells were plated in ultra-low attachment 96-well plates (Corning) and cultured in DMEM/F12 (Invitrogen) with growth factors, N-2, and B-27. 2B7 antibody (5 µg/mL) or control IgG was

added to the culture, and sphere formation was quantified after 10–14 days. For invasion and migration assays, 2×10^5 cells in serum-free medium with 2B7 antibody or control IgG were seeded into Transwell inserts. Matrigel®-coated inserts were used for invasion assays, while uncoated inserts were used for migration assays. The lower chamber was filled with RPMI-1640 medium with 10% FBS. After 24 h, migrated or invaded cells were stained and counted. For wound healing assays, A549 cells were grown to 80% confluence, scratched, and treated with 2B7 antibody or control IgG (5 μ g/mL). Wound closure was assessed after 24 h and calculated as: wound closure (%) = (1 – specific time wound width/initial wound width) × 100%.

Exosome analysis

A549 cells were cultured in RPMI medium until they reached 70-80% confluence. After washing with PBS, and incubated with exosome-free FBS medium (System Biosciences). After 48 h, conditioned medium was collected, and exosomes were isolated (System Biosciences), resuspended in PBS, quantified, and analyzed via exosome ELISA. For ELISA, mouse anti-CD63 antibody (200 ng/well) was coated onto Maxisorp 96-well plates and blocked with a protein-free blocking buffer (Thermo Fisher Scientific). Exosomes (100 µg) were added and incubated for 2 h at 37°C, followed by primary antibodies (anti-B7-H4, anti-PD-L1, or biotinylated anti-CD63) for 90 min. Detection was performed using HRP-conjugated anti-rabbit IgG antibody HRP-conjugated streptavidin (Sigma-Aldrich), and the reaction was visualized using Ultra-TMB solution.

Flow cytometry

Cells were dissociated using TrypLETM Express Enzyme (Gibco), filtered through 40 µm strainers, and fixed with 4% PFA for 15 min at 4°C. After washing with PBA buffer (1% BSA, 0.01% NaN₃ in PBS, pH 7.4), cells were incubated with mouse, chimeric, or humanized primary antibodies for 1 h at 4°C, followed by incubation with FITC-conjugated secondary antibodies for 30 min. For live-cell analysis, cells were stained with propidium iodide (PI; Sigma-Aldrich) and PI-negative cells were analyzed. Flow cytometry was performed using a FACSCalibur system (BD Biosciences), and the data were analyzed using CellQuest software.

Measurement of serum stability

Purified antibodies were incubated in 60% human serum at 37°C for up to 4 days. Samples were collected at 0, 3, 24, 48, 72, and 96 h, frozen at -80°C, and analyzed for binding activity to hTM4SF4

peptide-conjugated BSA (0.5 $\mu g/mL$) via indirect ELISA. The 0 h sample served as the baseline (100%) for comparison.

Antibody-dependent cell-mediated cytotoxicity (ADCC) assays

ADCC assays were performed using A549, THLE-2, MIA PaCa-2, and Huh-7 cells with the human FcγRIIIa (F158) Reporter Bioassay (Promega). Target cells were seeded into 96-well plates and incubated for 24 h, and the medium was replaced with ADCC assay buffer. Serially diluted antibodies and effector cells were added at effector-to-target (E:T) ratios of 12:1 or 20:1 and incubated for 6 h. Luminescence was measured using the Bio-Glo luciferase reagent and a GloMaxTM luminometer (Promega).

A549 xenograft and patient-derived xenograft experiments

A549 lung cancer cells (5 × 106) were injected subcutaneously into the right flank of the BALB/c nude mice. When the tumor reached approximately 50 mm³ or 200 mm³, the mice were randomized into control and treatment groups (n = 4 per group). Anti-TM4SF4 antibodies were administered either intratumorally (10 µg per mouse, six doses; total ~3 mg/kg) or intravenously (500 µg per mouse, two doses; total ~50 mg/kg). Control mice received IgG, and tumor growth was monitored every 2-3 days. For the PDX experiments, tumors with high TM4SF4 expression were transplanted into NOD scid gamma (NSG) mice. When tumors reached 100-150 mm³, mice (n = 4 per group) received intraperitoneal injections of 2B7, Hz2B7-1.2, control IgG (500 µg per mouse, two doses; total ~50 mg/kg) or cisplatin (250 ug per mouse, two doses; total ~25 mg/kg), administered at two-day intervals. The study was terminated when control tumors reached 1,000 mm³, with tumor measurements taken three times per week. The tumor volume was calculated using the following formula: (shortest diameter² × longest diameter)/2. All animal experiments IACUC-approved (KRIBB: KRIBB-AEC-19172, PDX: DNALINK 20-0107-S1A0 (2)). The PDX study was conducted at DNALINK (Korea).

Immunohistochemistry (IHC) of xenograft tumors

Formalin-fixed xenograft tumor tissues were paraffin-embedded, sectioned, and subjected to hematoxylin and eosin (H&E) staining as well as immunohistochemical staining. For IHC, tissue sections were deparaffinized, rehydrated, and stained with antibodies against CD44, E-cadherin (E-CAD),

and vimentin. Visualization was performed using a DAB detection kit (Abcam) according to the manufacturer's protocol. The stained slides were examined under a light microscope at 200× magnification, and representative images were captured. For each sample, at least seven non-overlapping fields of undamaged tumor tissue were selected and imaged. The DAB-stained areas were quantitatively analyzed using ImageJ software to measure staining intensity. Quantification results were statistically compared between the treatment and control groups.

Pharmacokinetic (PK) analysis in mice

For PK analysis of 2B7 antibody in A549 xenograft mice, 500 µg of 2B7 was administered intravenously on days -5 and 0 when the tumor size reached 50-200 mm³. Blood samples were collected at various time points, clotted at 25°C, and centrifuged at $2,000 \times g$ for 15 min at 4°C. The serum was then separated and stored at -80°C. Serum levels of the murine 2B7 antibody were determined by indirect ELISA using a standard curve. For PK analysis of Hz2B7-1.2 in BALB/c nude mice, Hz2B7-1.2 was via intraperitoneal administered injection 5-week-old female BALB/c nude mice at a dose of 500 μg per injection on Day -2 and Day 0. Blood samples were collected at various time points, clotted at 25°C, and centrifuged at $2,000 \times g$ for 15 min at 4°C. The serum was separated and stored at -80°C. The serum level of the Hz2B7-1.2 antibody was determined by human IgG ELISA using a standard curve. All animal procedures were conducted in accordance with the guidelines of the IACUC at Sejong Univ. (Approval No.: SJ-20220512).

Statistics and reproducibility

Statistical analyses were performed using GraphPad Prism, version 10.0. Data are presented as the mean \pm SEM from at least three independent experiments. Comparisons among groups were made using Student's t-test or one-way ANOVA, with p < 0.05 considered significant.

Results

Anti-hTM4SF4 mAbs were generated to target the LEL of hTM4SF4

We aimed to develop mAbs that bind to the extracellular region of TM4SF4 to inhibit its function and suppress cancer stemness in NSCLC. TM4SF4, a transmembrane protein consisting of 202 amino acids, has two extracellular loops, a small loop (SEL; amino

acids 31-45) and a large loop (LEL; amino acids 115-158) [49]. The SEL domain forms a small loop structure consisting of 15 amino acids, whereas the LEL domain forms a unique loop structure through disulfide bonds between two cysteine residues (C120 and C146) and two N-linked glycans at N124 and N156 (Figure 1A). When the TM4SF4 protein sequence was analyzed using the Kolaskar and Tongaonkar method [50], six epitope regions with high antigenicity were identified: amino acids 4-33, 53-67, 71-80, 92-116, 127-133, and 146-198. Among these, only 127-133 sequence is located within the extracellular loop, although partially masked by two N-glycan branches at N124 and N156. Considering the structural features, including N-glycosylation and disulfide bonds, the T126-E140 sequence was selected as the optimal epitope. It is centrally positioned within the C120-C146 loop, encompassing the predicted antigenic site (W127-D133), while avoiding the glycosylation site at N124 (Figure 1A). The selected 15-mer peptide, hTM4SF4 (T126-E140), was synthesized and conjugated to BSA using an SMCC crosslinker (Figure 1B). Splenocytes from mice hTM4SF4 immunized with the peptide-BSA conjugates were fused with myeloma cells to generate B-cell hybridomas. Screening of the hybridoma by ELISA using the immunizing antigen identified 50 hybridoma clones that produced antigen-specific antibodies. These hTM4SF4-specific clones were further evaluated by comparing their reactivity with hTM4SF4 peptide-conjugated BSA and BSA-SMCC (Figure S1A). This process identified approximately ten epitope-specific clones, which were further refined through repeated limiting dilution assays, ultimately yielding five stable clones: 2B7, 4C1, 8E2, 8E5, and 12A8. The isotypes of these antibodies were determined as IgG1, IgG2a, or IgG2b (Table S5). The antibodies were purified from the cell culture supernatant and analyzed using SDS-PAGE to confirm their purity (Figure S1B). The binding affinity of the purified antibodies to antigenic peptides was further assessed by ELISA using serial dilutions of the antibodies (Figure 1C). Among the five tested antibodies, 12A8 exhibited the highest reactivity for the hTM4SF4 peptide, followed by 2B7 and 4C1, whereas 8E2 and 8E5 showed lower reactivity. All antibodies successfully immunoprecipitated FLAG-tagged TM4SF4 expressed in HEK293T cells, confirming their reactivity with cellular TM4SF4 (Figure 1D; Figure S1C). Immunofluorescence analysis further demonstrated that the novel antibodies specifically recognized the extracellular domain of TM4SF4 on the cell membrane.

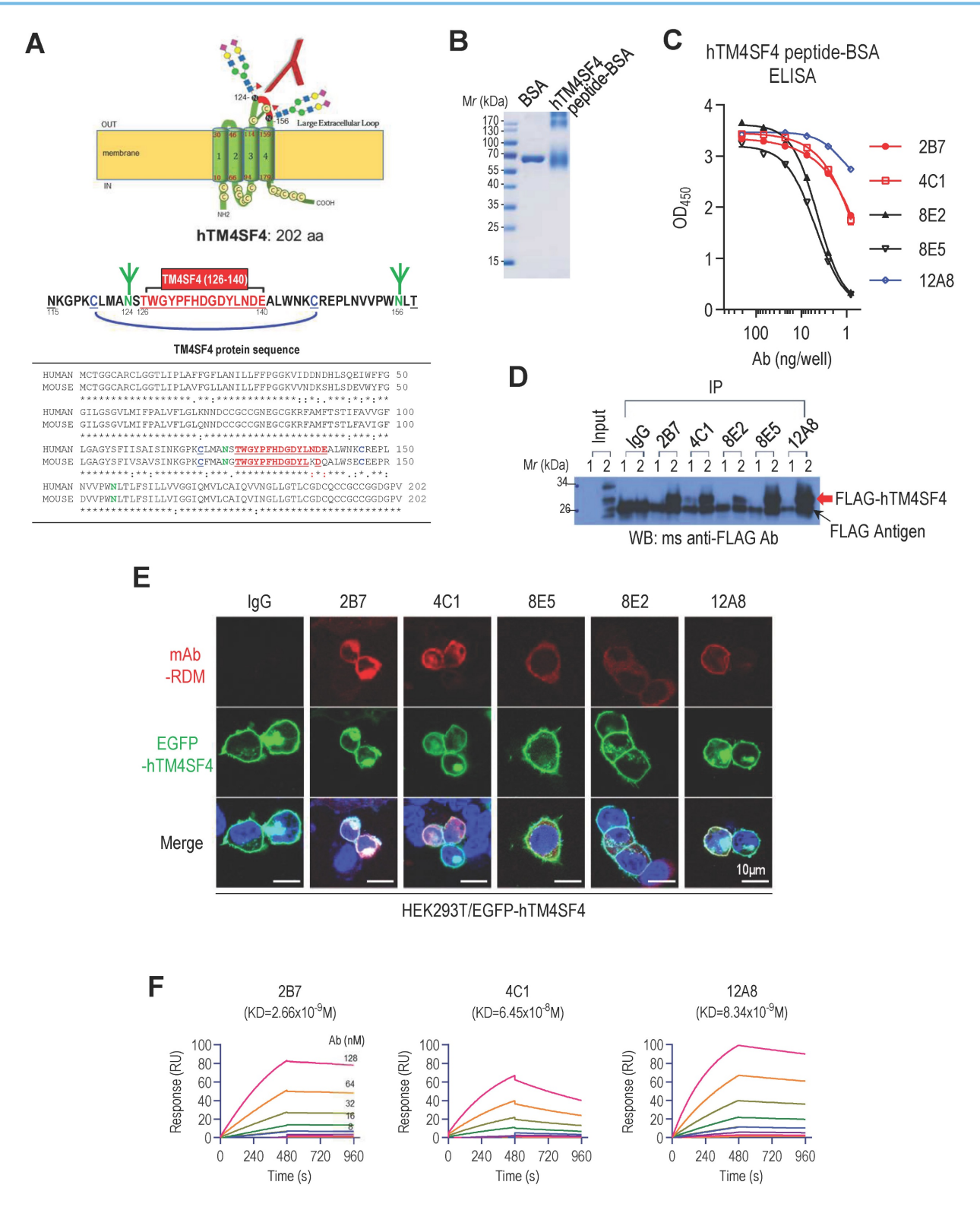


Figure 1. Development of Anti-hTM4SF4 Monoclonal Antibodies Using a 15-Mer Peptide Derived from the hTM4SF4 Extracellular Domain. A, Schematic representation of hTM4SF4 within the cell membrane, highlighting the selected antigenic epitope (T126–E140) in red within the LEL. B, The synthetic peptide hTM4SF4 (T126–E140) was conjugated to BSA using a Sulfo-SMCC crosslinker. Conjugation was confirmed via 10% SDS-PAGE under reducing conditions. C, ELISA results showing the binding affinity of five selected B-cell hybridoma clones, derived from mice immunized with the BSA-conjugated hTM4SF4 peptide. D, Immunoprecipitation of FLAG-tagged hTM4SF4 using the novel anti-hTM4SF4 monoclonal antibodies. HEK293T cells lysates transfected with FLAG-hTM4SF4 were immunoprecipitated with the antibodies, followed by western blot analysis with an anti-FLAG antibody. Mouse IgG was used as the control. E, Immunofluorescence analysis of hTM4SF4 expression in HEK293T cells using the novel antibodies. HEK293T cells transfected with EGFP-hTM4SF4 were subjected to immunofluorescence staining using the novel anti-hTM4SF4 antibodies, followed by a rhodamine-conjugated secondary antibody (top images). Merged images with EGFP-hTM4SF4 (middle images) show that the novel antibodies can access cell surface TM4SF4. Nuclei were counterstained with DAPI (blue). Scale bar, 10 µm. F, SPR sensorgrams showing the concentration-dependent binding kinetics of anti-hTM4SF4 antibodies to the hTM4SF4 peptide. The biotinylated peptide was immobilized on an SA sensor chip, and serially decreasing concentrations of the antibodies (128–1 nM) were applied. The equilibrium dissociation constants (K_D) are shown in each plot. Detailed kinetic parameters are provided in Table S6.

When EGFP-tagged TM4SF4 was expressed in HEK293T cells, probing with the novel antibodies followed by detection with rhodamine-conjugated secondary antibodies revealed colocalized fluorescent signals on the cellular membranes (Figure 1E, lower panel). Notably, stronger fluorescence signals were observed with antibodies 2B7 and 4C1, indicating their higher affinity for, or accessibility to, the target molecule. To confirm the binding of TM4SF4 to the surface of cancer cells, A549 cells were stained with novel antibodies. 2B7, 4C1, and 12A8 successfully cells, but stained A549 failed TM4SF4-knockdown A549 cells, demonstrating their binding specificity to TM4SF4 (Figure S1D). The binding affinities of the anti-hTM4SF4 mAb to the hTM4SF4 peptide were measured by SPR analysis. All three mAbs exhibited nanomolar binding affinities, indicating strong interactions with the epitope peptide, with 2B7 exhibiting the highest binding affinity (Figure 1F). Specifically, the equilibrium dissociation constants (KD) for 2B7, 4C1, and 12A8 were 2.66×10^{-9} M, 6.45×10^{-8} M, and 8.34×10^{-9} M, respectively (Figure 1F; Table S6).

Anti-hTM4SF4 mAbs effectively inhibit NSCLC growth in vitro and in vivo

To evaluate the therapeutic potential of anti-hTM4SF4 mAbs against NSCLC, their effects on tumor growth were assessed both in vitro and in vivo. In vitro colony formation assays demonstrated that anti-TM4SF4 mAb inhibited the proliferation of A549 lung cancer cells (Figure 2A). Notably, 2B7, 4C1, and 8E2 antibodies reduced cell proliferation by approximately 50%, exhibiting greater potency than 8E5 and 12A8. Xenograft experiments confirmed the antitumor efficacy of these antibodies in vivo. When A549 xenograft tumors reached approximately 50 mm³, anti-hTM4SF4 mAbs (2B7, 4C1, 8E2, and 12A8) were administered intratumorally, resulting in a significant reduction in tumor size in all treated mice (Figure 2B). Immunohistochemical analysis of tumor tissues injected with 2B7 revealed decreased expression of the cancer stem cell (CSC) marker CD44, as well as changes in the epithelial-mesenchymal transition (EMT) markers E-cadherin and vimentin (Figure 2C). A similar tumor reduction was also observed when the antibodies were administered to larger tumors (~200 mm³) (Figure S2A). In a separate xenograft model, 2B7, 4C1, and 12A8 antibodies were administered intravenously (Figure 2D; Figure S2B). For systemic administration, the antibody dose was increased approximately 16-fold. Among the tested mAbs, 2B7 and 4C1 significantly reduced tumor size, whereas 12A8 exhibited only marginal effects. In this case as well, tumor tissues from mice injected with

2B7 exhibited significant changes in CD44 and EMT marker expression (Figure 2E). When 2B7 antibody was administered intravenously, the number of injections was reduced, and the total antibody dose was split into two administrations. Despite this reduced dosing schedule, tumor growth was effectively suppressed. This finding suggests that the antibody maintained sufficient concentrations in tumor tissue to exert a sustained antitumor effect. To evaluate antibody persistence, serum levels of 2B7 were measured in xenograft mice using anti-TM4SF4 antibody ELISA (Figure 2F). Antibody activity decreased to approximately 50% within one-week post-injection and remained around 15% at 16 days. Nevertheless, tumor growth remained suppressed throughout the observation period, indicating that the antitumor activity of 2B7 was effectively sustained over time.

Collectively, these results demonstrate the significant therapeutic potential of novel anti-hTM4SF4 mAbs in suppressing NSCLC tumor growth both *in vitro* and *in vivo*. Among these, 2B7 and 4C1 exhibited the most potent antitumor effects, highlighting their potential as candidates for the development of targeted therapies against NSCLC. However, given that 2B7 demonstrated superior antigen-binding affinity than 4C1, subsequent experiments were primarily conducted using 2B7.

Anti-hTM4SF4 mAb, 2B7, inhibits self-renewal and EMT in NSCLC cells

We previously demonstrated that TM4SF4 is associated with CSC properties [28]. To determine whether the antitumor efficacy of anti-hTM4SF4 mAb due to the inhibition of TM4SF4-driven self-renewal, we examined changes in sphere and colony formation abilities following treatment with Treatment anti-hTM4SF4 mAbs. with significantly reduced the colony-forming capacity of A549 cells (Figure 3A) and markedly inhibited their sphere-forming ability (Figure 3B). Additionally, 2B7 treatment decreased the expression of self-renewal markers Sox2, Oct4, and β -catenin, and CSC markers ALDH1A1, ALDH1A3, and CD44 (Figure 3C). Immunocytochemistry further confirmed alterations in the expression of CD44 and ALDH1 following 2B7 treatment (Figure 3D).

TM4SF4 has also been implicated in EMT by activating receptor tyrosine kinase (RTK) and integrin-mediated signaling pathways that are critical for EMT, cancer stemness, and angiogenesis [28,51,52]. To evaluate whether 2B7 could inhibit TM4SF4-induced EMT, we examined its effects on cell invasion and migration. Treatment with 2B7 significantly reduced the invasion and migration of

A549 cells (**Figure 3E**) and impaired cell motility in the wound healing assays (**Figure 3F**). Furthermore, 2B7 treatment increased E-cadherin levels and reduced N-cadherin and vimentin expression, which are key EMT markers (**Figure 3G**). These findings were further validated by immunocytochemical analysis (**Figure 3H**). Additionally, 2B7 treatment reduced the expression of the EMT-regulating

transcription factors Snail, Twist, Slug, and Zeb1 (Figure 3I). 2B7 also suppressed the growth of another NSCLC cell line, Calu-3 (Figure 3J). Beyond NSCLC, 2B7 inhibited the growth of other TM4SF4-expressing cancer cell lines, including Huh7 (hepatocellular carcinoma) and MIA PaCa-2 (pancreatic cancer) (Figure 3K-L). These three tumor cell lines express substantial levels of TM4SF4 (Figure S3).

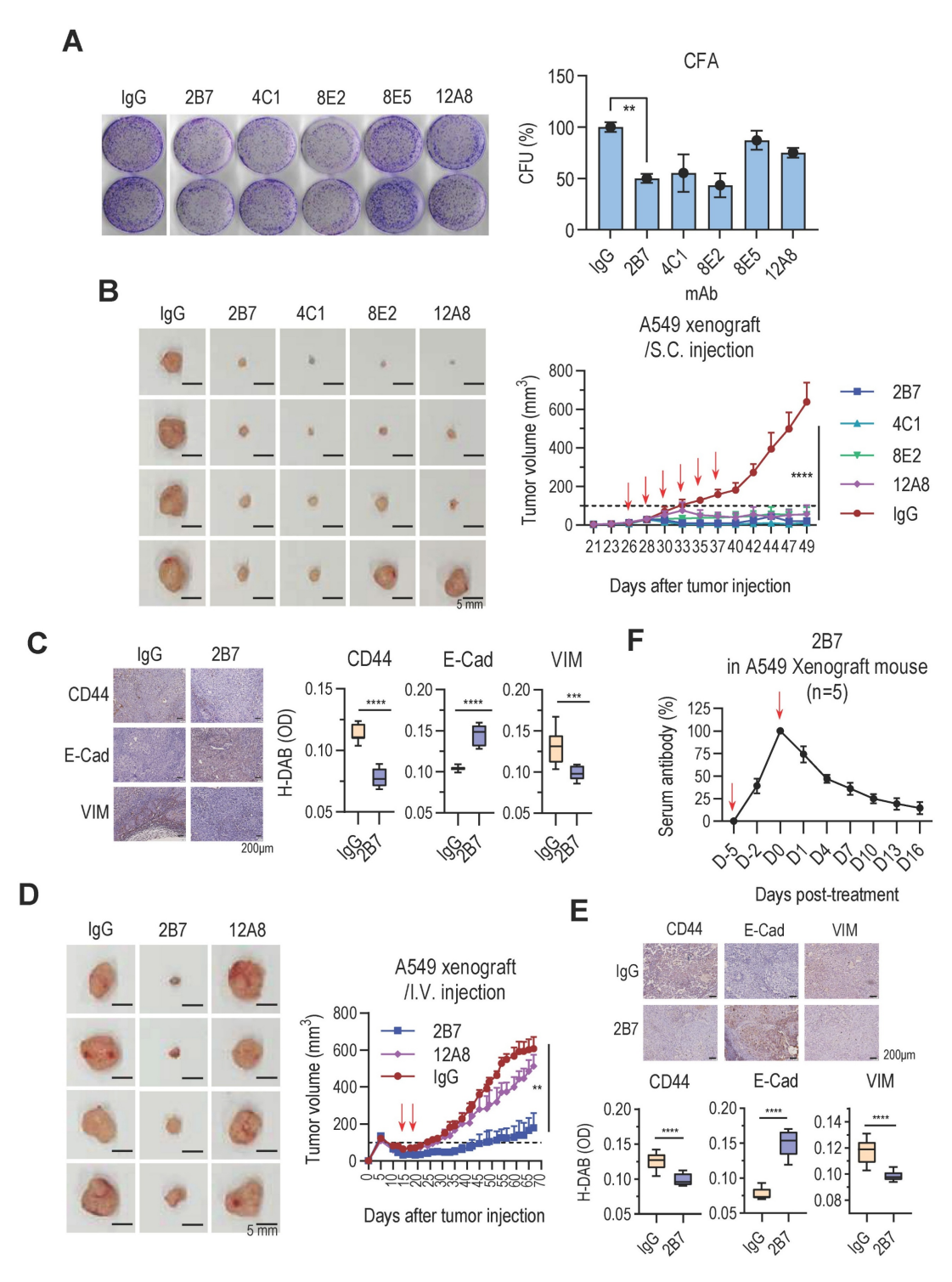


Figure 2. Novel Anti-hTM4SF4 mAbs Inhibit NSCLC Growth both In Vitro and In Vivo. **A,** Colony formation assay showing the inhibitory effects of anti-hTM4SF4 mAbs (2B7, 4C1, 8E2, 8E5, and 12A8) on A549 cells. Cells (3 × 10³ per well) were treated with 5 µg/mL of each antibody. Colony-forming units (CFUs) were quantified relative to control

wells treated with mouse IgG. **B,** Subcutaneous administration of anti-hTM4SF4 mAbs (2B7, 4C1, 8E2, and 12A8) inhibited tumor growth in an A549 NSCLC xenograft mouse model. Treatment commenced when tumor volume reached ~50 mm³. Antibodies were administered subcutaneously (10 μg per mouse per dose, six doses; total 60 μg per mouse) at 2-3-day intervals (red arrows). Tumor volumes were measured every 2-3 days and calculated as described in Methods. Tumors were excised and photographed on day 49. **C & E,** Immunohistochemical analysis of the cancer stem cell (CSC) marker CD44 and the epithelial–mesenchymal transition (EMT) markers E-cadherin and vimentin was performed on tumor tissues from mice injected with 2B7 or control IgG. Stained slides were examined under a light microscope at 200× magnification, and representative images were captured. DAB-stained areas were quantitatively analyzed using Image] software, and the results were statistically compared between the treatment and control groups. **D,** Intravenous administration of 2B7 and 12A8 further confirmed tumor growth inhibition. Antibodies were injected twice (500 μg per mouse per dose, total 1 mg per mouse) at 5-day intervals (red arrows). Tumors were excised and photographed at the end of the experiment. Scale bar, 5 mm. n = 4 per group. **F,** Serum levels of 2B7 in xenograft mice were quantified by ELISA using anti-TM4SF4 antigen and comparison to a standard curve. 2B7 activity measured 4 hours after injection was set as 100% reference for normalization

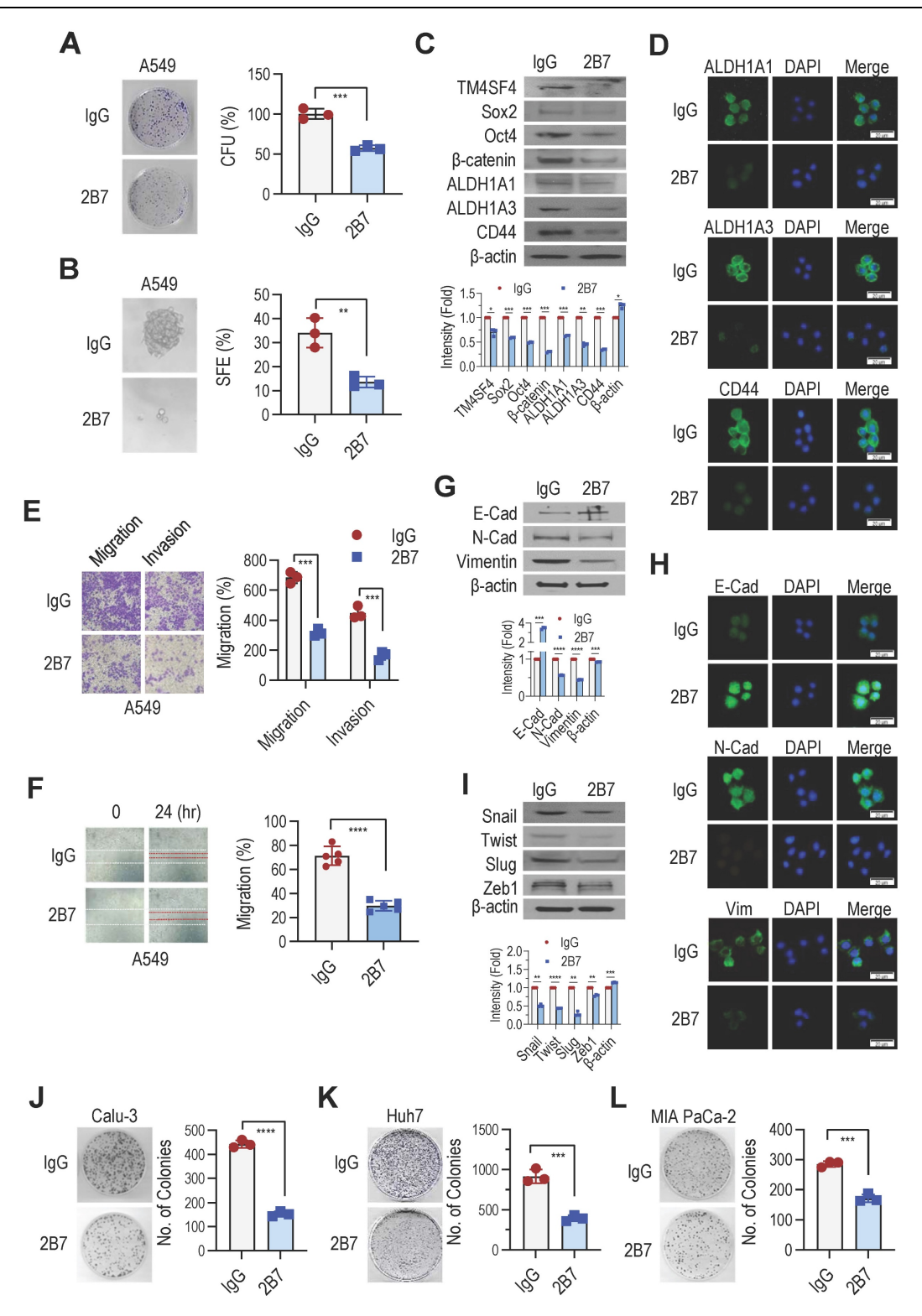


Figure 3. Anti-hTM4SF4 mAb 2B7 Suppresses Cancer Stemness, Migration, and Invasion in A549 NSCLC Cells and Other Cancer Models. **A,** Colony formation assay in A549 cells treated with 2B7 (5 μg/mL). Colonies were stained with crystal violet after 10 days. CFU percentages were calculated relative to mouse IgG controls. **B,** Sphere formation

assay in A549 cells treated with 2B7 (5 μ g/mL). Spheres were quantified and imaged (400× magnification) after 10–14 days. Sphere-forming efficiency (%) was calculated as spheres formed/total cells plated. **C**, Western blot analysis of CSC markers (Oct4, Sox2, β -catenin, ALDH1A1, ALDH1A3, and CD44) in A549 cells treated with 2B7 (5 μ g/mL) for 24 h. Band intensities were quantified using Image]. **D**, Immunocytochemistry of CSC markers (ALDH1A1, ALDH1A3, and CD44) in A549 cells treated with 2B7 (5 μ g/mL) for 24 h. Scale bar = 20 μ m. **E**, Migration and invasion assays of A549 cells treated with 2B7 (5 μ g/mL) for 24 h. Migrated/invaded cells were stained and quantified (400× magnification). Percentages were calculated relative to controls. **F**, Wound-healing assay in A549 cells treated with 2B7 (5 μ g/mL). Wound closure was imaged at 0 h and 24 h, and migration (%) was calculated as: (1- specific time wound width/initial wound width) × 100%. **G**, Western blot analysis of EMT markers (E-cadherin, N-cadherin, Vimentin) in A549 cells treated with 2B7 (5 μ g/mL) for 24 h. **H**, Immunocytochemistry of EMT markers (E-cadherin, N-cadherin, Vimentin) in A549 cells treated with 2B7 (5 μ g/mL) for 24 h. **J-L**, Colony formation assays in Calu-3 (NSCLC), Huh7 (hepatocellular carcinoma) and MIA PaCa-2 (pancreatic cancer) cells treated with 2B7 (5 μ g/mL). CFU percentages were calculated relative to controls.

Collectively, these findings demonstrate that the 2B7 antibody, which showed effective antitumor efficacy in NSCLC xenograft models, inhibited TM4SF4-mediated cancer stemness and EMT and provided evidence of its therapeutic potential in extrapulmonary cancer types.

2B7 Antibody inhibits feedback autocrine effects of IGF1 and OPN in NSCLC cells

TM4SF4 overexpression in A549 NSCLC cells activates IGF1R, increasing IGF1, OPN, and IL-1β [27,28]. This expression leads to IGF1Rβ phosphorylation and downstream activation of the PI3K/AKT/GSK3β and β-catenin pathways. OPN elevation further enhances CD44 activity, promoting EMT-related CSC traits via JAK2/STAT3 FAK/STAT3 pathways. To elucidate how 2B7 inhibits the cancer cell proliferation, self-renewal, and metastasis, we examined its effects on TM4SF4-related signaling pathways. 2B7 treatment reduced IGF1Rβ phosphorylation, lowering IL-1β, OPN, and IGF1 levels (**Figure 4A**). This disrupted PI3K/AKT/GSK3β and β-catenin signaling (Figure 4B). Reduced OPN CD44 diminished activation, EMT-associated cancer stemness via JAK2/STAT3 and FAK/STAT3 pathways (Figure 4C). Overall, these results highlight the potential of 2B7 as a therapeutic antibody for NSCLC by suppressing key cancer stemness and EMT pathways (Figure 4D).

Signaling pathways activated by IGF1 and OPN, known to enhance EMT and CSC-like properties, also contribute to the resistance to chemotherapy and radiotherapy [53-55]. To assess whether 2B7 could overcome this resistance, we evaluated its effects in combination with other antitumor treatments. A549 cells treated with 2B7 following y-irradiation showed a synergistic reduction in colony formation compared to controls (Figure 4E). Additionally, 2B7 treatment significantly enhanced A549 cell sensitivity to gefitinib, effectively reducing drug resistance (Figure **4F**). These results suggest that 2B7 is not only effective as a standalone antitumor agent but also enhances therapeutic efficacy when combined with radiotherapy or targeted therapy by suppressing CSC properties and overcoming treatment resistance.

PD-L1(B7-H1) and B7-H4, key ICLs, are overexpressed in tumors, suppressing T-cell activation and facilitating immune evasion [7-9,56,57]. B7-H4, abundant in lung cancer, is associated with IGF1R signaling [58], while PD-L1 expression is regulated bv OPN from tumor-associated macrophages [59]. Our studies revealed that TM4SF4 upregulation enhanced OPN and IGF1 secretion in lung cancer cells [28], suggesting its role in modulating ICL expression. Therefore, targeting TM4SF4 may reduce ICL expression by decreasing extracellular IGF1 and OPN levels, thereby improving the efficiency of cancer therapies. Consistent with this hypothesis, TM4SF4 suppression via siRNA or 2B7 treatment reduced PD-L1 and B7-H4 levels (Figure 4G-H). Neutralizing OPN/IGF1 TM4SF4-overexpressing cells had similar effects (Figure 4I-J), with all treatments also reducing TM4SF4 levels. Overall, these results highlight the dual role of 2B7 in inhibiting TM4SF4-mediated cancer stemness and limiting immune evasion by suppressing ICL expression.

Exosomes derived from NSCLC cells are also known to carry PD-L1 and B7-H4, contributing to immunosuppression and tumor progression by further reducing T cell activity [60–62]. 2B7 treatment of A549 cells significantly lowered PD-L1 and B7-H4 levels in exosomes, as confirmed by sandwich ELISA (**Figure 4K**). These results indicate that 2B7 not only suppresses ICL expression in cancer cells but also reduces exosomal ICL levels, potentially enhancing antitumor immune responses.

Humanized 2B7 antibodies were constructed and characterized

As demonstrated, 2B7 exhibits potent antitumor efficacy by targeting TM4SF4. However, murine antibodies face clinical limitations due to their immunogenicity in humans [63]. To overcome this challenge and enhance its clinical applicability, the murine 2B7 antibody was engineered into a humanized form, a process that reduces immunogenicity while preserving antigen specificity and therapeutic efficacy.

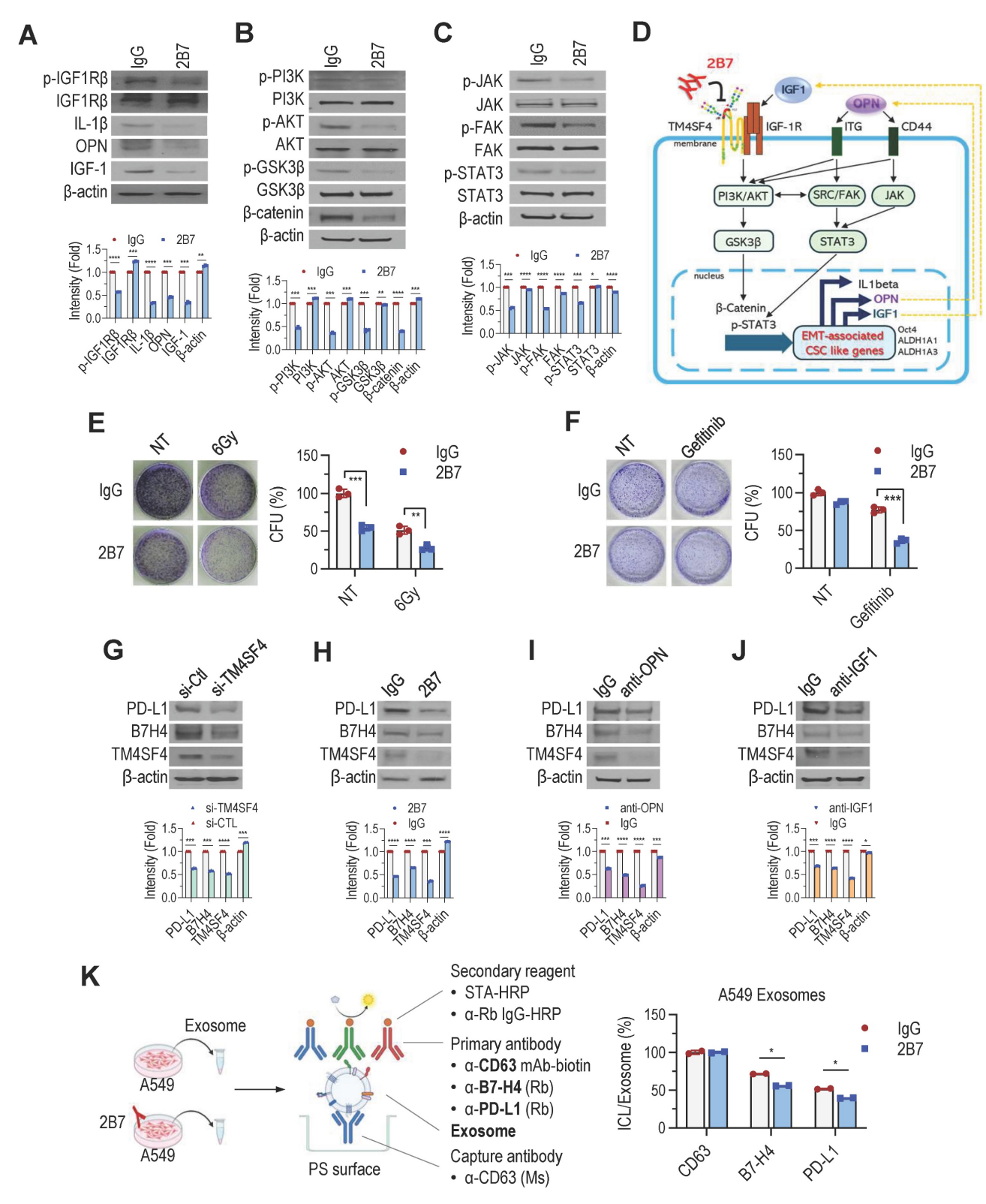


Figure 4. 2B7 Inhibits the Feedback Autocrine Effects of IGF1 and OPN, Enhancing the Sensitivity of NSCLC Cells to Antitumor Therapy. **A-D**, Suppression of TM4SF4-associated signaling by 2B7 (5 μg/mL) in A549 cells. **A**, IGF1Rβ phosphorylation and autocrine cytokines (IGF1, OPN, IL-1β) were reduced. **B**, Pl3K/AKT/GSK3β pathway (downstream of IGF1R) was inhibited. **C**, JAK (FAK)/STAT3 pathway (downstream of OPN/CD44) was suppressed. **D**, Schematic model depicting 2B7-mediated inhibition of EMT-associated CSC-like properties via disruption of TM4SF4/IGP1 and TM4SF4/OPN autocrine loops and suppression of downstream signaling. **E-F**, Colony formation assays assessing therapy sensitization. **E**, γ-Irradiation (6 Gy) + 2B7 (5 μg/mL). Colony formation was significantly reduced compared to irradiation alone. **F**, Gefitinib (1 μg/mL) + 2B7 (5 μg/mL). Combined treatment showed synergistic inhibition of colony formation. **G-J**, PD-L1 and B7-H4 expression analyses in A549 Cells after treatments. **G**, TM4SF4 knockdown by siRNA (48 h post-transfection). **H**, 2B7 treatment (5 μg/mL, 24 h). **I**, OPN-neutralizing antibody treatment. **J**, IGF1-neutralizing antibody treatment. Mouse IgG was used as the control for all antibody treatments. **K**, Quantification of exosomal PD-L1 and B7-H4 by sandwich ELISA: Tumor-derived exosomes were captured using anti-CD63 (exosome marker). Exosomal PD-L1 and B7-H4 were detected using anti-PD-L1 or anti-B7-H4 rabbit antibodies, followed by anti-rabbit IgG-HRP. Total exosome response.

We first defined the CDR sequence of 2B7 (Figure S4) and constructed an expression vector for the chimeric antibody (Chi2B7) that combines the variable regions of the murine 2B7 antibody with the constant regions of human IgG1 and the k light chain (Figure S5). Human IgG1, the most commonly used isotype in therapeutic antibodies, is preferred for its ability to induce ADCC and Complement-Dependent Cytotoxicity (CDC). The k chain was selected for its prevalence and lower immunogenicity. The Chi2B7 expression vector was transfected into HEK293T cells and the recombinant antibody Chi2B7 was purified from culture supernatants (Figure S6A-B). Functional validation showed that Chi2B7 retained the antitumor efficacy of the original murine antibody. ELISA confirmed specific binding of Chi2B7 to the TM4SF4 peptide-BSA, but not to BSA (Figure S6C). Additionally, flow cytometry analysis demonstrated that Chi2B7 effectively recognized and bound to cell surface TM4SF4 in NSCLC cell lines A549 and Calu-3 (Figure S6D).

To develop a humanized version of the 2B7 antibody, we generated genes encoding the CDRs of the 2B7 antibody grafted onto the framework regions of the human antibody 3QRG, which showed the highest sequence homology to the 2B7 VH and Vk regions (Figure 5A, see Methods for details). The resulting humanized 2B7 VH (Hz2B7-1.0) and Vk (Hz2B7-0.1) genes were subcloned into pdCMV-dhfr vector, generating the Hz2B7-1.1 expression construct (Figure S5). The pdCMV-dhfr-Hz2B7-1.1 vector was transfected into HEK293T cells, and the humanized antibodies were successfully produced (Figure S7). To enhance the antigen-binding affinity of Hz2B7-1.1, the antigen-antibody binding interface was analyzed in detail using docking simulations. Since the 3D structure of 2B7 has not yet been experimentally determined, homology modeling was performed using the X-ray crystal structure of the chimeric antibody X836 (PDB ID: 3MBX) as a template [43]. A structural model of the hTM4SF4 (T126-E140) epitope was generated by energy minimization of the linear peptide. The antigen-antibody interface and binding affinity were then evaluated using the homology-modeled structure of 2B7 and epitope model. As shown in Figure 5B (left panel), the peptide epitope fits well within the CDR of Hz2B7-1.1, with a calculated binding free energy of -11.6 kcal/mol, indicating a more thermodynamically favorable interaction compared to the 2B7-peptide complex (-11.2 kcal/mol; **Figure 5B**, right panel) and the 4C1peptide complex (-10.3 kcal/mol; Figure S8). Based on structural analysis of the Hz2B7-1.1-peptide interface, residue substitutions were explored,

targeting positions moderately distant from the epitope to avoid disrupting direct interactions. Key residues identified were Asn31L and Thr100L in the light chain (Vκ), and Trp54H, Trp55H, and Asn56H in the heavy chain VH. Notably, Trp55H was positioned at a moderate distance from Asp133 in the epitope. It was hypothesized that substituting Trp55H with hydrogen bond-donating amino acids, such as Ser or Tyr, would strengthen antibodyepitope interactions (Figure 5B, middle panel). These substitutions produced two VH domain variants: W55S (Hz2B7-3.0) and W55Y (Hz2B7-4.0) (Figure 5A, upper panel). To further enhance the hydrophobic interactions between Hz2B7 and the epitope, Asn31L in the Vk region was targeted, as its modification could improve interactions with Trp127 and Phe131 of the epitope. Substitution of Asn31L with Val or Phe generated hydrophobic variants: N31V (Hz2B7-0.2) and N31F (Hz2B7-0.3) (Figure 5A, lower panel). To further optimize binding affinity, single VH and Vk mutants were combined to form double mutants: Hz2B7-3.2 and Hz2B7-3.3 (W55S + N31F/N31V); Hz2B7-4.2 and Hz2B7-4.3 (W55Y + N31F/N31V). The resulting pdCMV-dhfr-Hz2B7-1.1 variants were transfected into HEK293T cells for antibody production (Figure S7). Indirect ELISA revealed that all nine Hz2B7 variants specifically bound the TM4SF4 peptide-BSA, outperforming the chimeric (**Figure** 5C). Hz2B7-1.2 Chi2B7 (Vκ N31F) demonstrated the strongest binding activity, followed by Hz2B7-1.3 (Vk N31V) and Hz2B7-1.1. SPR analysis confirmed these results, with Hz2B7-1.2 showing the highest affinity ($K_D = 6.03 \times 10^{-9}$ M). In contrast, Hz2B7-1.1, chimeric 2B7, and Hz2B7-4.3 displayed K_{DS} of 2.442 × 10⁻⁸ M, 6.074 × 10⁻⁸ M, and 8.165 × 10⁻⁸ M, respectively (Figure 5D; Figure S9; Table S7). Flow cytometry confirmed that all humanized antibodies had enhanced binding to cell surface TM4SF4 in A549 and Calu-3 cells compared to Chi2B7 (Figure 5E). Hz2B7-1.2 showed the strongest binding in A549 cells, outperforming Hz2B7-1.1 and Hz2B7-1.3, though the difference was not significant in Calu-3 cells. Additionally, Hz2B7-1.2 bound to HCC cell lines (Huh7, SNU-387, SNU-449) but not to primary human hepatocytes (hPH) (Figure S10), suggesting potential for clinical application in HCC.

To evaluate *in vitro* serum stability, Hz2B7-1.2 was incubated in 60% human serum at 37 °C (**Figure 5F**). The binding activity remained stable over 96 h, independent of the production cell line (HEK293T or CHO). Comparable stability was observed for Hz2B7-1.1 and the murine 2B7 antibody, indicating that Hz2B7-1.2 is structurally stable in human serum.

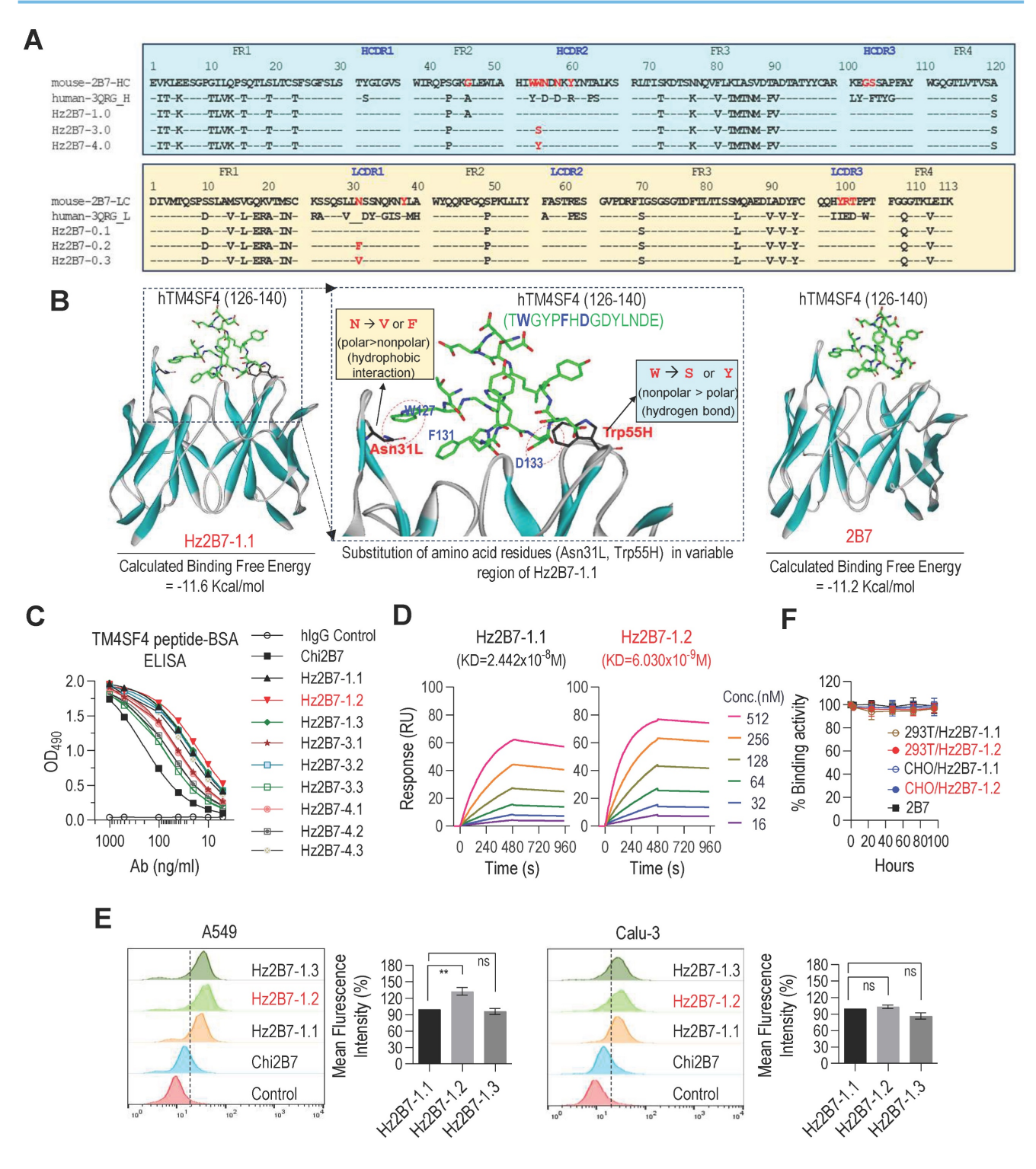


Figure 5. Construction and Characterization of Humanized 2B7 Antibodies. A, Comparison of murine 2B7, human 3QRG, and humanized 2B7 antibody sequences. Heavy chain (VH) sequences shown in the upper panel; light chain (VK) sequences in the lower panel. Key mutations in the humanized variants are indicated. B, Docking Simulation of Epitope–Antibody Interaction: Docked pose of the hTM4SF4 epitope within the CDRs of 2B7 and Hz2B7-1.1. CDRs displayed in ribbon representation; epitope shown as stick models. Dotted circles indicate hydrophobic interactions and hydrogen bonds at the binding interface. C, Binding affinity analysis of chimeric and humanized 2B7 antibodies to hTM4SF4 peptide-BSA via indirect ELISA. Hz2B7-1.2 (Vx N31F) exhibited the highest binding affinity among all tested antibodies. Human IgG served as the negative control. D, SPR Analysis of concentration-dependent binding kinetics of humanized 2B7 antibodies to hTM4SF4 peptide. Biotinylated hTM4SF4 (T126–E140) peptide was immobilized on an SA sensor chip, and serially decreasing concentrations of the antibodies (512–16 nM) were applied. KD values were presented on each sensorgram, with detailed kinetics listed in Table S7. E, Comparison of binding activity of humanized 2B7 antibodies to NSCLC cell lines (A549 and Calu-3) by flow cytometry. Relative binding was determined based on mean fluorescence intensities obtained from flow cytometric analysis. Data are presented as mean values ± SD (n = 3). ns, not significant. **, p < 0.01. F, Serum stability of murine 2B7, Hz2B7-1.1, and Hz2B7-1.2 antibodies. Antibodies incubated in 60% human serum at 37°C and evaluated by indirect ELISA for binding activity to hTM4SF4 peptide-BSA. All antibodies produced from CHO or HEK293T cells retained binding activity for up to 96 hours.

Hz2B7-1.2 exhibits anti-cancer effects and mediates cellular cytotoxicity against TM4SF4-expressing cancer cells

The antitumor efficacy of the humanized Hz2B7-1.2 antibody was evaluated in vitro and in vivo, alongside its murine counterpart, 2B7. In colony formation assays, both antibodies similarly inhibited A549 cell growth at equivalent concentrations (Figure 6A). Additionally, both antibodies suppressed the growth of other cancer cell lines, including Calu-3 (NSCLC; Figure S11A), Huh7 (hepatocellular carcinoma; Figure S11A), and MIA PaCa-2 (pancreatic cancer; Figure 6A). Treatment with Hz2B7-1.2 in these cells reduced cellular TM4SF4 expression (Figure S11B), indicating effective binding of the antibody to tumor cells. Cell cycle changes were also assessed following treatment with TM4SF4 antibodies. siRNA-mediated knockdown of TM4SF4 resulted in a marked increase in the G0/G1 phase and a corresponding decrease in the S phase (Figure S12A-C). Treatment with the Hz2B7-1.2 antibody also induced cell cycle alterations; although the effect was less pronounced than with siRNA knockdown, a moderate decrease in the S phase was observed (Figure S12D-E).

In spheroid formation assays using Calu-3 (lung cancer) and Huh7 (liver cancer) cell lines, spheroid formation reduced by over 50% following treatment with either antibody (Figure 6B). Additionally, Hz2B7-1.2 enhanced the radiosensitivity of A549 cells, showing effects comparable to murine 2B7 (Figure 6C; Figure 4E). Hz2B7-1.2 treatment also modulates the expression of CSC- and EMT-related markers. Immunofluorescence analysis showed a reduction in CSC markers (CD44, ALDH1A1, and ALDH1A3) and alterations in EMT markers, including increased E-cadherin and decreased N-cadherin and Vimentin, in response to Hz2B7-1.2 treatment (Figure 6D). To quantify the changes in EMT markers and TM4SF4 expression, Western blot analyses were performed and results were quantified relative to the controls (Figure 6E).

Therapeutic antibodies exert antitumor effects through both Fab-mediated target inhibition and Fc-mediated effector functions. A critical mechanism, ADCC, depends on antibody binding to target antigens and the recruitment of cytotoxic immune cells (NK cells, macrophages, monocytes). Trastuzumab (anti-HER2) is a well-established ADCC-inducing antibody [64], while ADCP plays a vital role in the efficacy of antibodies like rituximab and daratumumab [65-67]. To assess the ADCC potential of Hz2B7-1.2 (IgG1 isotype) against TM4SF4-positive A549 cells, we performed an ADCC

assay using FcγRIIIa (F158)-expressing effector cells. Hz2B7-1.2 induced a dose-dependent ADCC response, effectively activating effector cells (**Figure 7A**). Hz2B7-1.2 exhibited higher ADCC activity than the chimeric Chi2B7 antibody at equivalent doses, likely due to enhanced TM4SF4 binding (Table S7). The control antibody showed no cytotoxicity under the same conditions. Additionally, Hz2B7-1.2 induced robust ADCC in MIA PaCa-2 (pancreatic cancer) and Huh7 (hepatocellular carcinoma) (**Figure 7B**), but not in THLE-2 (normal liver cells), confirming its specificity for TM4SF4-expressing cancer cells (Figure S3).

The in vivo antitumor efficacy of Hz2B7-1.2, a humanized antibody combining the superior TM4SF4-targeting ability of 2B7 with the effector functions of IgG1, was evaluated. In the A549 xenograft model, intratumoral injections of Hz2B7-1.2 significantly inhibited tumor growth (Figure 7C). Intravenous administration of Hz2B7-1.2 also reduced tumor size (Figure 7D); however, its antitumor effect was less pronounced than that of the murine 2B7 antibody (Figure 2D). Immunohistochemical analysis reflected these results, showing changes in CSC and EMT markers after administration of the humanized antibody; however, these effects were less marked than those observed with the murine antibody (Figure 7E-F). To determine whether the reduced antitumor efficacy of Hz2B7-1.2 following intravenous injection was related to its in vivo instability, we conducted a serum stability assessment in BALB/c mice after intraperitoneal injection. The serum concentration of Hz2B7-1.2 began to decline four days post-injection, reaching ~50% of initial levels by day 16 (**Figure 7G**). The observed half-life and clearance were considered moderate, given that natural IgG1 antibodies typically exhibit a half-life of ~3 weeks and monoclonal IgG1 antibodies display a broad half-life range (6-32 days) [68]. Thus, the reduced efficacy of Hz2B7-1.2 is unlikely due to serum instability. To further assess its therapeutic efficacy, Hz2B7-1.2 and murine 2B7 were evaluated in a TM4SF4-expressing lung cancer PDX (Figure S13). Both antibodies model administered via intraperitoneal injection (total dose of 50 mg/kg), matching the A549 xenograft model. The control group received cisplatin (total dose of 25 mg/kg), close to the lethal threshold. While murine 2B7 achieved tumor suppression comparable to cisplatin, Hz2B7-1.2 led to only a modest tumor size reduction (Figure 7H).

Collectively, these results demonstrate that the humanized Hz2B7-1.2 antibody successfully grafted and preserved the superior TM4SF4 target-binding properties of the parental murine 2B7 antibody. Additionally, as an IgG1 isotype, Hz2B7-1.2

effectively mediates antibody-dependent cellular cytotoxicity (ADCC) against TM4SF4-expressing cancer cells, resulting in tumor clearance. However, its antitumor efficacy was significantly lower than that of the murine 2B7 antibody in the tumor mouse model. This reduced efficacy is likely due to structural

and functional differences between the murine and humanized antibodies, particularly the effector cell recruitment functions introduced in the IgG1-type humanized antibody, which are absent in the murine IgG1 antibody.

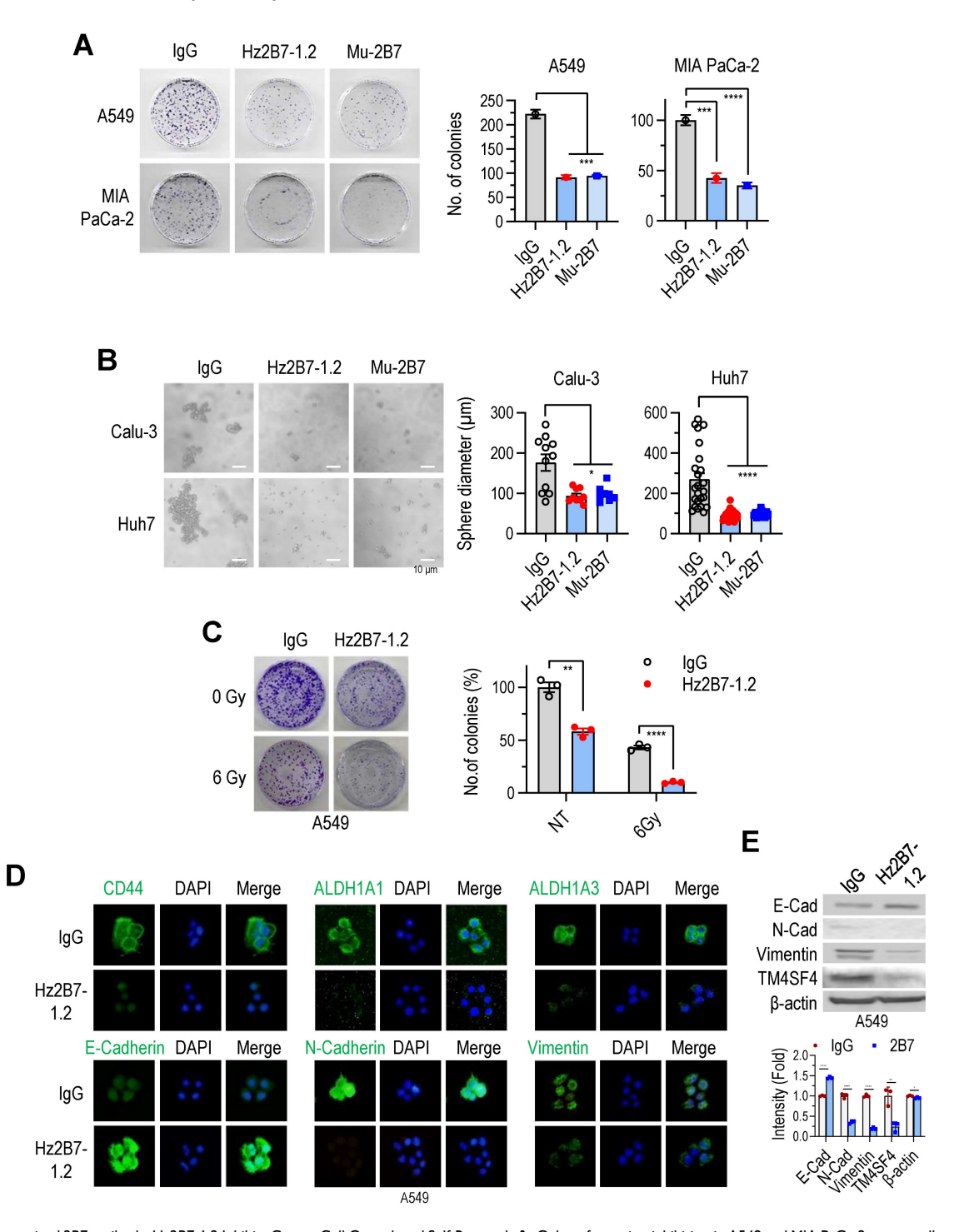


Figure 6. Humanized 2B7 antibody, Hz2B7-1.2 Inhibits Cancer Cell Growth and Self-Renewal. **A,** Colony formation inhibition in A549 and MIA PaCa-2 cancer cells treated with Hz2B7-1.2 (5 μg/mL). Human IgG was used as a control, and murine 2B7 was included for comparison. CFU percentages were calculated relative to the IgG control. **B,** Inhibition of sphere formation in Calu-3 NSCLC cells and Huh-7 HCC cells treated with Hz2B7-1.2 (5 μg/mL). Spheres diameters were measured after 14 days (n ≥ 8). **C,** Radiosensitization effect of Hz2B7-1.2 in A549 cells treated with 5 μg/mL antibody following 6 Gy γ-irradiation. Colony formation was quantified. Data are presented as mean ± SEM. **, p < 0.01; ***, p < 0.001; ***, p < 0.001; ***, p < 0.001. **D,** Immunocytochemical analysis of cancer stemness markers (CD44, ALDHIA1, and ALDHIA3) and EMT markers (E-cadherin, N-cadherin, and Vimentin) in A549 cells treated with Hz2B7-1.2 (5 μg/mL) for 24 h. Scale bar = 20 μm. **E,** Western blot analysis of EMT markers and TM4SF4 expression in Hz2B7-1.2-treated A549 cells. Results were quantified relative to controls.

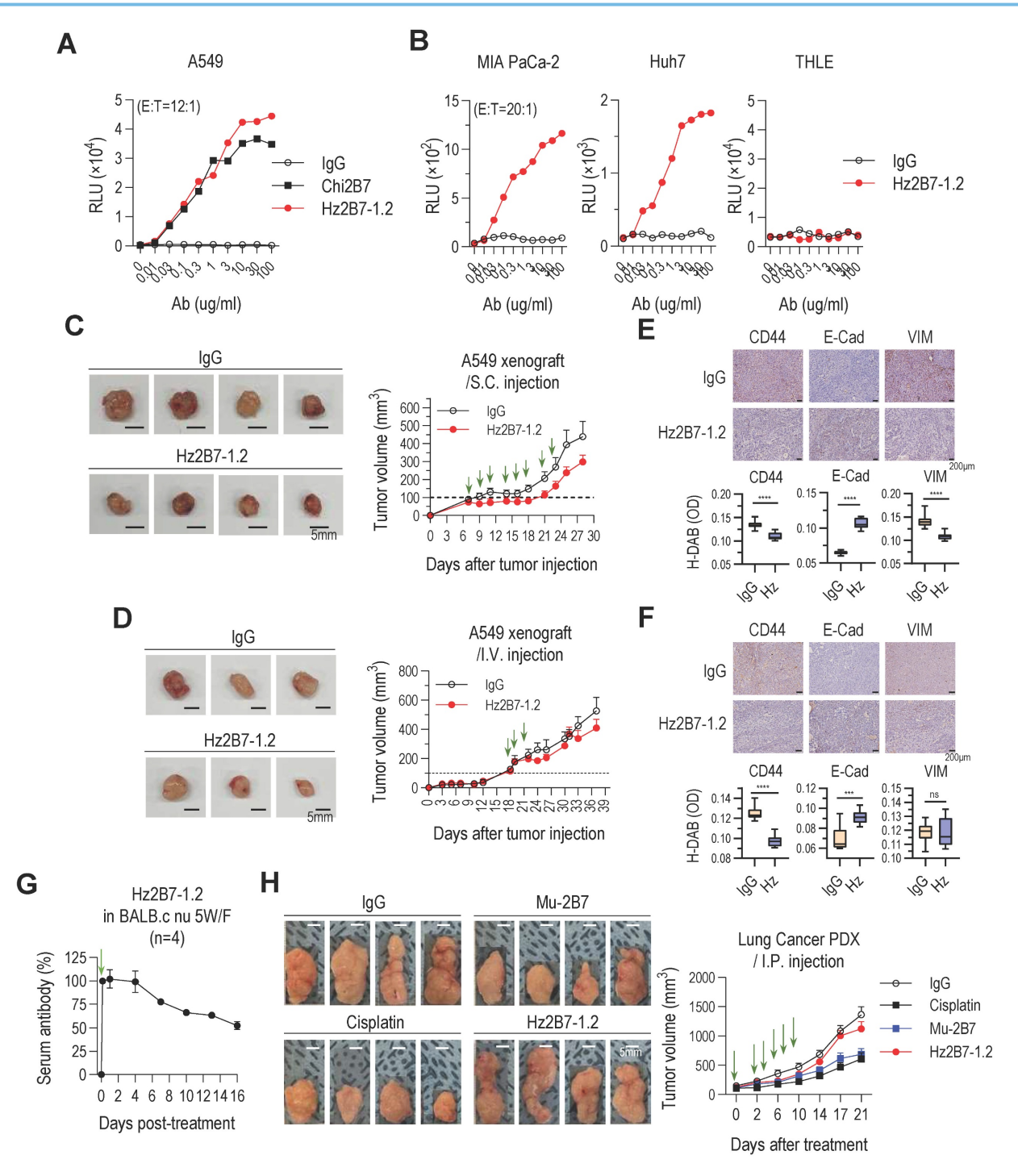


Figure 7. Hz2B7-1.2 Mediates Cellular Cytotoxicity and Inhibits Tumor Growth in TM4SF4-Expressing Tumors. A, ADCC activity against A549 cells. The hFcyRIIIa (F158) ADCC reporter assay was performed. Effector cells were co-cultured with A549 NSCLC cells at an E:T ratio of 12:1 in the presence of serially diluted antibodies for 6 h. Luminescence detection was conducted to assess ADCC activity. Human IgGI was used as a negative control, and Chi2B7 was tested for comparison. B, ADCC activity in other cancer cell lines. The ADCC assay was repeated using MIA PaCa-2, Huh7 cancer cells, and THLE-2 non-tumorigenic liver epithelial cells. Effector cells were incubated with target cells (E:T = 20:1) in the presence of serially diluted antibodies for 6 h. Hz2B7-1.2 induced dose-dependent ADCC in cancer cells but showed no cytotoxicity in THLE-2 cells, highlighting tumor specificity. C, Tumor growth inhibition in A549 xenograft model after subcutaneous administration. Hz2B7-1.2 (10 µg/mouse/dose) was subcutaneously administered eight times at 2–3 day intervals (total 80 µg/mouse). Treatment started when tumor size reached ~100 mm³. Tumor growth was monitored every 2–3 days, and tumors were excised for imaging at the end of the study. Scale bar = 5 mm; n = 4 per group. D, Intravenous administration in A549 xenograft model. Hz2B7-1.2 (500 µg/mouse/dose) was intravenously injected three times at 3-day intervals (total 1.5 mg/mouse). Tumor volume was measured throughout the study. n = 3 per group. E&F, Immunohistochemical analysis of CD44, E-cadherin and vimentin was performed on tumor tissues from mice injected with Hz2B7-1.2 or control IgG (E: subcutaneous, F: intravenous injection). Stained slides were examined under a light microscope at 200× magnification, and representative images were captured. DAB-stained areas were quantitatively analyzed using Image] software, and results were statistically compared between the treatment and control groups. G, PK analysis of Hz2B7-1.2 in mice. 5-week-old female BALB/c nude mice were administered 500 µg Hz2B7-1.2 intraperitoneally on Day -2 and Day 0. Serum samples were collected at specified time points, and Hz2B7-1.2 concentrations were quantified using a human IgG ELISA based on a standard curve. n = 4 per group. H, Tumor growth in a PDX model treated with anti-hTM4SF4 antibodies (2B7 and Hz2B7-1.2). High TM4SF4-expressing patient lung tumor tissues were transplanted into NSG mice. Treatments were administered intraperitoneally when the average tumor size reached 100–150 mm³, included anti-hTM4SF4 mAbs (2B7 and Hz2B7-1.2), control lgG, and cisplatin. Each of the treatment groups received six injections at two-day intervals (green arrows). The total dosages were 50 mg/kg for the antibody and 25 mg/kg for cisplatin. Tumor size was measured every four days, and the experiment was terminated when the tumor size in the control group reached 1,000 mm³. n = 4 per group

Discussion

A major challenge in cancer therapy is the selective elimination of cancer cells while sparing normal tissues. To overcome this, targeted therapies have been developed, with monoclonal antibodies playing a pivotal role due to their high specificity for tumor-associated antigens. In particular, target-specific antibodies against molecules such as TM4SF4, which is highly expressed in cancer stem cells, are expected to make significant contributions to antitumor strategies. In this study, we successfully generated monoclonal antibodies against TM4SF4-a transmembrane protein overexpressed in lung cancer cells-through immunization of mice with a short antigenic peptide derived from its LEL domain. Although concerns existed regarding glycan-mediated shielding of the targeted epitope, located between two proximal N-glycan structures, in vitro experiments confirmed sufficient antibody accessibility. The central location of the epitope within a loop structure formed by two cysteine residues, with minimal conformational complexity, enabled a short linear peptide to elicit high-affinity antibodies. Importantly, antibody binding to this region effectively modulated TM4SF4 function, highlighting its therapeutic potential.

Among the novel anti-TM4SF4 monoclonal antibodies developed, 2B7-a murine IgG1 antibody with a κ light chain – demonstrated robust antitumor effects in both in vitro and in vivo lung cancer models. 2B7 markedly inhibited key malignant phenotypes, including cell growth, stemness, migration, invasion, and radiation resistance. Despite the generally low FcyR affinity of murine IgG1 [69], 2B7 exhibited potent antitumor efficacy, likely through direct blockade of TM4SF4 signaling, a crucial regulator of cancer stemness. Notably, this study is the first to show that TM4SF4 signaling promotes immune checkpoint ligand (ICL) expression, facilitating immune evasion. Treatment with 2B7 effectively suppressed ICL expression in both cancer cells and exosomes, thereby enhancing antitumor immunity.

To translate 2B7 for clinical use, we engineered a humanized version, Hz2B7-1.2 (human IgG1 subclass), via CDR grafting and affinity maturation. SPR and cell-based assays demonstrated that Hz2B7-1.2 retained antigen-binding affinity after humanization. Serum stability studies showed that Hz2B7-1.2 remained sufficiently stable *in vivo*. However, while *in vitro* efficacy persisted, the *in vivo* antitumor activity of Hz2B7-1.2 was reduced, particularly following systemic administration. Since both 2B7 and Hz2B7-1.2 bind TM4SF4 equivalently *in*

vitro, this difference is likely attributable to variations in Fc-mediated interactions.

Murine immune cells can respond to both murine and humanized antibodies, allowing for partial assessment of ADCC and other Fc-dependent functions in mouse models. Human IgG1 antibodies can engage murine Fcy receptors (FcyRI and FcyRIII) with differing affinities to induce ADCC, whereas murine IgG2a and IgG2b isotypes display even stronger ADCC due to higher FcyRIII affinity [70]. In contrast, the murine IgG1 isotype exhibits weaker effector function. In our study, 2B7 – due to low FcyR affinity-likely remained predominantly as free antibody in mouse circulation, facilitating direct targeting and high antitumor efficacy. Conversely, Hz2B7-1.2 is expected to interact more efficiently with FcyRs, leading to immune complex formation and reduced free antibody levels, potentially limiting antigen accessibility and antitumor potential (Figure S14). IgG1 antibodies generally have a molecular weight of approximately 150 kDa and a size of 10-14 nm; by comparison, immune complexes formed with immune cells can exceed this size by several orders of magnitude. While sufficient antigen accessibility enables Fc-mediated cytotoxicity by humanized IgG1 antibodies, epitope shielding by glycans may restrict efficacy to only those capable of accessing the target site.

Under *in vitro* settings without immune cells, both 2B7 and Hz2B7-1.2 directly bind the cancer cell antigen, yielding similar effects; in vivo, their engagement with immune cells diverges, explaining differences in efficacy. Murine antibodies 4C1 and 12A8, although similar to 2B7 in antigen binding, showed reduced antitumor efficacy, likely due to their high Fc γ R affinity that limits free antibody levels for direct targeting.

Enhancing Hz2B7-1.2 efficacy will require preservation of Fab-mediated target binding, reduction of FcyR engagement to maintain higher free antibody levels, and retention of FcRn affinity for optimal serum stability. Potential strategies include Fc glycan modification or switching subclasses to IgG2 or IgG4 [71,72], minimizing immune cell interactions successfully demonstrated in therapeutics [73]. Future research will focus on such optimization of Hz2B7-1.2 to maximize its clinical potential. Given the demonstrated effectiveness of 2B7 in hepatocellular and pancreatic cancer models, anti-TM4SF4 monoclonal antibody therapy may be broadly applicable to other TM4SF4-overexpressing tumors, supporting the development of universal CSC-targeted cancer therapies.

Abbreviations

ADCC: antibody-dependent cellular cytotoxicity; CDC: complement-dependent cytotoxicity; CDRs: complementarity-determining regions; CSCs: cancer stem cells; EMT: epithelial-mesenchymal transition; FR: framework region; HAMA: human anti-mouse antibody; ICIs: immune checkpoint inhibitors; ICL: immune checkpoint ligand; IGF1: insulin-like growth factor 1; LEL: large extracellular loop; mAbs: monoclonal antibodies; MET: mesenchymal-to-epithelial transition; MTX: methotrexate; NSCLC: non-small cell lung cancer; OPN: osteopontin; PDX: patient-derived xenograft; SEL: small extracellular loop; SPR: surface plasmon resonance; TM4SF4: transmembrane 4 superfamily member 4.

Supplementary Material

Supplementary figures and tables. https://www.thno.org/v16p1762s1.pdf

Acknowledgements

This study was supported by the Nuclear Research & Development Program of the National Research Foundation of Korea (NRF) grant (NRF-2018M2A2B3A02072343) funded by the Korean government, the Ministry of Science, ICT & Future Planning (MSIP), and the Korea Research Institute of Bioscience & Biotechnology (KRIBB) Research Initiative Program (KGM9942522).

Availability of data and materials

The data and materials used in this study are available from the corresponding author upon reasonable request.

Contributions

Rae-Kwon Kim: Investigation, methodology, formal analysis, writing-original draft. Chang-Kyu **Heo:** Investigation, methodology, writing-original draft. Mun Ju Choi: Investigation, Formal analysis, writing-original draft. Yeon-jee Kahm: Investigation, Visualization. Min Kyu Kim: Investigation. Minyong Lee: Investigation. Ji Yoon Lee: Investigation. Hwang Seo Park: Investigation, methodology, writingoriginal draft. Uhee Jung: Validation. Byung-Chul Shin: Supervision. Bum-Jin Kim: Supervision. Sung-Chul Kim: Supervision. Eun-Wie Cho: Conceptualization, supervision, writing-review, and Chun Jeih **Ryu:** Conceptualization, supervision, writing-review, and editing. In-Gyu Kim: Conceptualization, project administration, funding acquisition, writing—review, and editing.

Competing Interests

The authors have declared that no competing interest exists.

References

- Kratzer TB, Bandi P, Freedman ND, Smith RA, Travis WD, Jemal A, et al. Lung cancer statistics, 2023. Cancer 2024;130:1330-48.
- Hendriks LEL, Remon J, Faivre-Finn C, Garassino MC, Heymach JV, Kerr KM, et al. Non-small-cell lung cancer. Nat Rev Dis Primers 2024;10:71.
- Leon G, MacDonagh L, Finn SP, Cuffe S, Barr MP. Cancer stem cells in drug resistant lung cancer: Targeting cell surface markers and signaling pathways. Pharmacol Ther 2016;158:71-90.
- Chen J, Lu W, Chen M, Cai Z, Zhan P, Liu X, et al. Efficacy of immunotherapy in patients with oncogene-driven non-small-cell lung cancer: a systematic review and meta-analysis. Ther Adv Med Oncol. 2024;16:17588359231225036.
- Zhou S, Yang H. Immunotherapy resistance in non-small-cell lung cancer: From mechanism to clinical strategies. Front Immunol 2023;14:1129465.
 Salem A, Asselin MC, Reymen B, Jackson A, Lambin P, West CML, et al.
- Salem A, Asselin MC, Reymen B, Jackson A, Lambin P, West CML, et al. Targeting Hypoxia to Improve Non-Small Cell Lung Cancer Outcome. J Natl Cancer Inst 2018;110.
- Han Y, Liu D, Li L. PD-1/PD-L1 pathway: current researches in cancer. Am J Cancer Res 2020;10:727-42.
- Santoni M, Romagnoli E, Saladino T, Foghini L, Guarino S, Capponi M, et al. Triple negative breast cancer: Key role of Tumor-Associated Macrophages in regulating the activity of anti-PD-1/PD-L1 agents. Biochim Biophys Acta Rev Cancer 2018;1869:78-84.
- Sui H, Ma N, Wang Y, Li H, Liu X, Su Y, et al. Anti-PD-1/PD-L1 Therapy for Non-Small-Cell Lung Cancer: Toward Personalized Medicine and Combination Strategies. J Immunol Res 2018;2018:6984948.
- Ni L, Dong C. New B7 Family Checkpoints in Human Cancers. Mol Cancer Ther 2017;16:1203-11.
- Mortezaee K. B7x in cancer immunity and immunotherapy. Int Immunopharmacol 2023;118:110133.
- Carlino MS, Larkin J, Long GV. Immune checkpoint inhibitors in melanoma. Lancet 2021;398:1002-14.
- Li JX, Huang JM, Jiang ZB, Li RZ, Sun A, Lai-Han Leung E, et al. Current Clinical Progress of PD-1/PD-L1 Immunotherapy and Potential Combination Treatment in Non-Small Cell Lung Cancer. Integr Cancer Ther 2019;18:1534735419890020.
- Wang JY, Wang WP. B7-H4, a promising target for immunotherapy. Cell Immunol 2020;347:104008.
- Blando J, Sharma A, Higa MG, Zhao H, Vence L, Yadav SS, et al. Comparison of immune infiltrates in melanoma and pancreatic cancer highlights VISTA as a potential target in pancreatic cancer. Proc Natl Acad Sci USA 2019;116:1692-97.
- Mortezaee K. Enriched cancer stem cells, dense stroma, and cold immunity: Interrelated events in pancreatic cancer. J Biochem Mol Toxicol 2021;35:e22708.
- Jiang Y, Zhan H. Communication between EMT and PD-L1 signaling: New insights into tumor immune evasion. Cancer Lett 2020;468:72-81.
- Su S, Lin A, Luo P, Zou J, Huang Z, Wang X, et al. Effect of mesenchymal-epithelial transition amplification on immune microenvironment and efficacy of immune checkpoint inhibitors in patients with non-small cell lung cancer. Ann Transl Med 2021;9:1475.
- Rouzbahani E, Majidpoor J, Najafi S, Mortezaee K. Cancer stem cells in immunoregulation and bypassing anti-checkpoint therapy. Biomed Pharmacother 2022;156:113906.
- Robert JH, Amoussou NG, Mai HL, Logé C, Brouard S. Tetraspanins: useful multifunction proteins for the possible design and development of small-molecule therapeutic tools. Drug Discov Today. 2021;26:56-68.
- Lee SA, Lee SY, Cho IH, Oh MA, Kang ES, Kim YB, et al. Tetraspanin TM4SF5 mediates loss of contact inhibition through epithelial-mesenchymal transition in human hepatocarcinoma. J Clin Invest 2008;118:1354-66.
- Allioli N, Vincent S, Vlaeminck-Guillem V, Decaussin-Petrucci M, Ragage F, Ruffion A, et al. TM4SF1, a novel primary androgen receptor target gene over-expressed in human prostate cancer and involved in cell migration. Prostate 2011;71:1239-50.
- 23. Tang Q, Chen J, Di Z, Yuan W, Zhou Z, Liu Z, et al. TM4SF1 promotes EMT and cancer stemness via the Wnt/ β -catenin/SOX2 pathway in colorectal cancer. J Exp Clin Cancer Res 2020;39:232.
- Cai S, Deng Y, Peng H, Shen J. Role of Tetraspanins in Hepatocellular Carcinoma. Front Oncol. 2021;11:723341.
- Huang MY, Wang HM, Chang HJ, Hsiao CP, Wang JY, Lin SR. Overexpression of S100B, TM4SF4, and OLFM4 genes is correlated with liver metastasis in Taiwanese colorectal cancer patients. DNA Cell Biol 2012;31:43-9.
- Wang L, Feng J, Da L, Li Y, Li Z, Zhao M. Adenovirus-mediated delivery of siRNA targeting TM4SF4 attenuated liver cancer cell growth in vitro and in vivo. Acta Biochim Biophys Sin (Shanghai) 2013;45:213-9.
- Choi SI, Kim SY, Lee J, Cho EW, Kim IG. TM4SF4 overexpression in radiation-resistant lung carcinoma cells activates IGF1R via elevation of IGF1. Oncotarget 2014;5:9823-37.

- Choi SI, Kim SY, Lee JH, Kim JY, Cho EW, Kim IG. Osteopontin production by TM4SF4 signaling drives a positive feedback autocrine loop with the STAT3 pathway to maintain cancer stem cell-like properties in lung cancer cells. Oncotarget 2017:8:101284-97.
- Jin W. Role of JAK/STAT3 Signaling in the Regulation of Metastasis, the Transition of Cancer Stem Cells, and Chemoresistance of Cancer by Epithelial-Mesenchymal Transition. Cells 2020;9:217.
- Kelley B. The history and potential future of monoclonal antibody therapeutics development and manufacturing in four eras. MAbs. 2024;16:2373330.
- Ecker DM, Jones SD, Levine HL. The therapeutic monoclonal antibody market. MAbs 2015;7:9-14.
- Crescioli S, Kaplon H, Chenoweth A, Wang L, Visweswaraiah J, Reichert JM. Antibodies to watch in 2024. MAbs 2024;16:2297450.
- Shawler DL, Bartholomew RM, Smith LM, Dillman RO. Human immune response to multiple injections of murine monoclonal IgG. J Immunol 1985:135:1530-5.
- Jones PT, Dear PH, Foote J, Neuberger MS, Winter G. Replacing the complementarity-determining regions in a human antibody with those from a mouse. Nature 1986;321:522-5.
- Al-Lazikani B, Lesk AM, Chothia C. Standard conformations for the canonical structures of immunoglobulins. J Mol Biol 1997;273:927-48.
- Queen C, Schneider WP, Selick HE, Payne PW, Landolfi NF, Duncan JF, et al. A humanized antibody that binds to the interleukin 2 receptor. Proc Natl Acad Sci USA 1989:86:10029-33.
- Simons JF, Lim YW, Carter KP, Wagner EK, Wayham N, Adler AS, et al. Affinity maturation of antibodies by combinatorial codon mutagenesis versus error-prone PCR. MAbs 2020;12:1803646.
- Kim JH, Gripon P, Bouezzedine F, Jeong MS, Chi SW, Ryu SE, et al. Enhanced humanization and affinity maturation of neutralizing anti-hepatitis B virus preS1 antibody based on antigen-antibody complex structure. FEBS Lett 2015;589:193-200.
- Urlaub G, Käs E, Carothers AM, Chasin LA. Deletion of the diploid dihydrofolate reductase locus from cultured mammalian cells. Cell 1983;33:405-12.
- Wang Z, Raifu M, Howard M, Smith L, Hansen D, Goldsby R, et al. Universal PCR amplification of mouse immunoglobulin gene variable regions: the design of degenerate primers and an assessment of the effect of DNA polymerase 3' to 5' exonuclease activity. J Immunol Methods 2000;233:167-77.
- Yoon SO, Lee TS, Kim SJ, Jang MH, Kang YJ, Park JH, et al. Construction, affinity maturation, and biological characterization of an anti-tumor-associated glycoprotein-72 humanized antibody. J Biol Chem 2006;281:6985-92.
- Altschul SF, Madden TL, Schäffer AA, Zhang J, Zhang Z, Miller W, et al. Gapped BLAST and PSI-BLAST: a new generation of protein database search programs. Nucleic Acids Res 1997;25:3389-402.
- 43. Teplyakov A, Obmolova G, Carton JM, Gao W, Zhao Y, Gilliland GL. On the domain pairing in chimeric antibodies. Mol Immunol 2010;47:2422-6.
- Thompson JD, Higgins DG, Gibson TJ. CLUSTAL W: improving the sensitivity
 of progressive multiple sequence alignment through sequence weighting,
 position-specific gap penalties and weight matrix choice. Nucleic Acids Res
 1994:22:4673-80.
- Sali A, Blundell TL. Comparative protein modelling by satisfaction of spatial restraints. J Mol Biol 1993;234:779-815.
- Fiser A, Do RK, Sali A. Modeling of loops in protein structures. Protein Sci 2000;9:1753-73.
- Morris GM, Goodsell DS, Halliday RS, Huey R, Hart WE, Belew RK, et al. Automated docking using a Lamarckian genetic algorithm and an empirical binding free energy function. Journal of Computational Chemistry 1998:19:1639-62.
- Park H, Jung HY, Kim K, Kim M, Hong S. Rational Computational Design of Fourth-Generation EGFR Inhibitors to Combat Drug-Resistant Non-Small Cell Lung Cancer. Int J Mol Sci. 2020;21:9323.
- Rahim NS, Wu YS, Sim MS, Velaga A, Bonam SR, Gopinath SCB, et al. Three Members of Transmembrane-4-Superfamily, TM4SF1, TM4SF4, and TM4SF5, as Emerging Anticancer Molecular Targets against Cancer Phenotypes and Chemoresistance. Pharmaceuticals (Basel) 2023;16:110.
- Kolaskar AS, Tongaonkar PC. A semi-empirical method for prediction of antigenic determinants on protein antigens. FEBS Lett 1990;276:172-4.
- Butti R, Das S, Gunasekaran VP, Yadav AS, Kumar D, Kundu GC. Receptor tyrosine kinases (RTKs) in breast cancer: signaling, therapeutic implications and challenges. Mol Cancer 2018;17:34.
- Vu T, Datta PK. Regulation of EMT in Colorectal Cancer: A Culprit in Metastasis. Cancers (Basel) 2017;9:171.
- Kothari AN, Arffa ML, Chang V, Blackwell RH, Syn WK, Zhang J, et al. Osteopontin-A Master Regulator of Epithelial-Mesenchymal Transition. J Clin Med 2016;5:39.
- 54. Kim IG, Lee JH, Kim SY, Hwang HM, Kim TR, Cho EW. Hypoxia-inducible transgelin 2 selects epithelial-to-mesenchymal transition and y-radiation-resistant subtypes by focal adhesion kinase-associated insulin-like growth factor 1 receptor activation in non-small-cell lung cancer cells. Cancer Sci 2018;109:3519-31.
- Ngo MT, Jeng HY, Kuo YC, Diony Nanda J, Brahmadhi A, Ling TY, et al. The Role of IGF/IGF-1R Signaling in Hepatocellular Carcinomas: Stemness-Related Properties and Drug Resistance. Int J Mol Sci 2021;22:1931.

- Lu Y, Wu F, Cao Q, Sun Y, Huang M, Xiao J, et al. B7-H4 is increased in lung adenocarcinoma harboring EGFR-activating mutations and contributes to immunosuppression. Oncogene 2022;41:704-17.
- John P, Wei Y, Liu W, Du M, Guan F, Zang X. The B7x Immune Checkpoint Pathway: From Discovery to Clinical Trial. Trends Pharmacol Sci 2019:40:883-96.
- Zhao Z, Zhang N, Li A, Zhou B, Chen Y, Chen S, et al. Insulin-like growth factor-1 receptor induces immunosuppression in lung cancer by upregulating B7-H4 expression through the MEK/ERK signaling pathway. Cancer Lett 2020;485:14-26.
- Li Y, Liu H, Zhao Y, Yue D, Chen C, Li C, et al. Tumor-associated macrophages (TAMs)-derived osteopontin (OPN) upregulates PD-L1 expression and predicts poor prognosis in non-small cell lung cancer (NSCLC). Thorac Cancer 2021;12:2698-709.
- Kim DH, Kim H, Choi YJ, Kim SY, Lee JE, Sung KJ, et al. Exosomal PD-L1 promotes tumor growth through immune escape in non-small cell lung cancer. Exp Mol Med 2019;51:1-13.
- Chen G, Huang AC, Zhang W, Zhang G, Wu M, Xu W, et al. Exosomal PD-L1 contributes to immunosuppression and is associated with anti-PD-1 response. Nature. 2018;560:382-86.
- Tian Y, Liu C, Li Z, Ai M, Wang B, Du K, et al. Exosomal B7-H4 from irradiated glioblastoma cells contributes to increase FoxP3 expression of differentiating Th1 cells and promotes tumor growth. Redox Biol 2022:56:102454.
- Lu RM, Hwang YC, Liu IJ, Lee CC, Tsai HZ, Li HJ, et al. Development of therapeutic antibodies for the treatment of diseases. J Biomed Sci 2020;27:1.
- Baselga J, Albanell J, Molina MA, Arribas J. Mechanism of action of trastuzumab and scientific update. Semin Oncol 2001;28:4-11.
- Shi Y, Fan X, Deng H, Brezski RJ, Rycyzyn M, Jordan RE, et al. Trastuzumab triggers phagocytic killing of high HER2 cancer cells in vitro and in vivo by interaction with Fcγ receptors on macrophages. J Immunol 2015;194:4379-86.
- VanDerMeid KR, Elliott MR, Baran AM, Barr PM, Chu CC, Zent CS. Cellular Cytotoxicity of Next-Generation CD20 Monoclonal Antibodies. Cancer Immunol Res 2018;6:1150-60.
- van de Donk NWCJ, Usmani SZ. CD38 Antibodies in Multiple Myeloma: Mechanisms of Action and Modes of Resistance. Front Immunol 2018;9:2134.
- Paul S, Konig MF, Pardoll DM, Bettegowda C, Papadopoulos N, Wright KM, et al. Cancer therapy with antibodies. Nat Rev Cancer 2024;24:399-426.
- Stewart R, Hammond SA, Oberst M, Wilkinson RW. The role of Fc gamma receptors in the activity of immunomodulatory antibodies for cancer. J Immunother Cancer 2014;2:29.
- Overdijk MB, Verploegen S, Ortiz Buijsse A, Vink T, Leusen JH, Bleeker WK, et al. Crosstalk between human IgG isotypes and murine effector cells. J Immunol 2012;189:3430-8.
- Yu J, Song Y, Tian W. How to select IgG subclasses in developing anti-tumor therapeutic antibodies. J Hematol Oncol 2020;13:45.
- Braster R, Bögels M, Benonisson H, Wuhrer M, Plomp R, Bentlage AEH, et al. Afucosylated IgG Targets FcyRIV for Enhanced Tumor Therapy in Mice. Cancers (Basel). 2021;13:2372.
- 73. Jiang Y, Chen M, Nie H, Yuan Y. PD-1 and PD-L1 in cancer immunotherapy: clinical implications and future considerations. Hum Vaccin Immunother 2019;15:1111-22.